Low-Frequency Variability of the Tropical Atlantic Surface Topography: Altimetry and Model Comparison

S. Arnault, A. Morlière, and J. Merle

Laboratoire d'Océanographie Dynamique et de Climatologie, ORSTOM, Université Pierre et Marie Curie, Paris

Y. Ménard

Groupe de Recherche en Géodésie Spatiale, Centre National d'Etudes Spatiales, Toulouse, France

Altimetric data, climatological hydrological data, and numerical model results are compared over the tropical Atlantic Ocean between November 1986 and November 1988. All reproduce the seasonal cycle of the dynamic topography rather well, and the agreement is particularly good between altimetry and the primitive equation model. The study of the 1986–1988 period reveals interannual events evidenced by both the altimetry and the models, especially during spring 1988 in the Gulf of Guinea.

1. Introduction

The present (Tropical Ocean and Global Atmosphere) and future (World Ocean Circulation Experiment) oceanographic programs are now devoted to the long-term climate forecasting. As a matter of fact, the success of these programs in terms of climate predictability at scales of several months to decades relies on the implementation of new techniques to provide global observations of surface parameters and currents for monitoring the oceans. During the last decades, historical merchant ship bathythermograph (BT) profiles and extensive oceanographic experiments have evidenced the large spectrum of the oceanic variability, especially in the upper layers of the tropical Atlantic [*Lass et al.*, 1987; *Hisard and Hénin*, 1987; *Katz*, 1987]. However, oceanographic cruises have, for technical and funding reasons, so limited duration and spatial coverage that it is difficult to resolve large spatial and temporal scales.

In recent years, two different methods of monitoring the oceans have been explored by oceanographers. The first method is modeling. This can range from process models, generally used to isolate a specific oceanic phenomenon [*Cane and Sarachik*, 1981; *Busalacchi and Picaut*, 1983; *du Penhoat and Gouriou*, 1987], to three-dimensional complex models used to obtain a more realistic simulation of the oceans [*Philander and Pacanowski*, 1986; *Leetmaa and Ji*, 1989; *Morlière et al.*, 1989].

The second method is using spatial techniques to obtain a global quasi-synoptic view of the whole ocean. Three generations of altimeters (Skylab, GEOS 3, and Seasat) have already demonstrated the ability of altimetric data to study surface circulation [*Cheney et al.*, 1983; *Douglas et al.*, 1983; *Fu*, 1983; *Ménard*, 1983; *Daniault and Ménard*, 1985], even if looking at large-scale signal through altimetry is more challenging than mesoscale studies because of the possible overlap by altimetric long wavelength errors: orbit, atmospheric, and oceanic [*Musman*, 1986; *Malarde et al.*, 1987; *Miller et al.*, 1986; *Périgaud et al.*, 1986].

More recently, in the tropical Atlantic Ocean, *Arnault et*

al. [1990] found good agreement between the seasonal variability of the dynamic topography as observed from historical hydrographic data [*Merle and Arnault*, 1985] and from altimetric data, but a qualitative and quantitative comparison between altimetry and models over a basinwide scale and a 2-year cycle is still missing. This is the topic of this paper. Section 2 gives the data processing and the two model descriptions. Then, in section 3 we focus on the seasonal cycle of the tropical Atlantic before approaching the interannual variability (section 4). Discussions and conclusions follow in section 5.

2. Data Processing and Models

The Data

Altimetric data. We considered in this paper the Geosat 17.05-day Exact Repeat Mission data over the tropical Atlantic Ocean between 60°W–20°E and 20°N–20°S, from November 1986 to November 1988, about 118 repetitive tracks of 43 passes. At the equator the orbit tracks are about 150 km apart and along a single track; the distance between two measurements is 7 km.

As noted by *Cheney et al.* [1987], Fleet Numerical Oceanographic Center (FNOC) wet and dry tropospheric corrections [*Saastamoinen*, 1972; *Tapley et al.*, 1982] and ionospheric corrections based on the Global Positioning System climatic ionosphere model were applied. The tidal signals were removed according to the tide models of *Cartwright and Taylor* [1971] and *Schwiderski* [1980].

The absence of a well-known geoid for such a large-scale study leads to a time variability interpretation. Three different methods can be used to extract the variability signal from the altimetric data: the crossover differences have given encouraging results in the tropical Pacific [*Miller et al.*, 1986], as has the use of a mean sea surface in the Atlantic [*Ménard*, 1988]. The collinear profile method we used here was previously tested with success in a mesoscale study of the northwest Atlantic region [*Ménard*, 1983] and in the Pacific [*Musman*, 1986; *Malarde et al.*, 1987]. An analysis of this method has been described in detail by *Arnault et al.* [1990]. The altimetric measurements of the sea surface are first resampled and adjusted along the track (60-km spacing
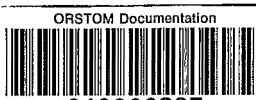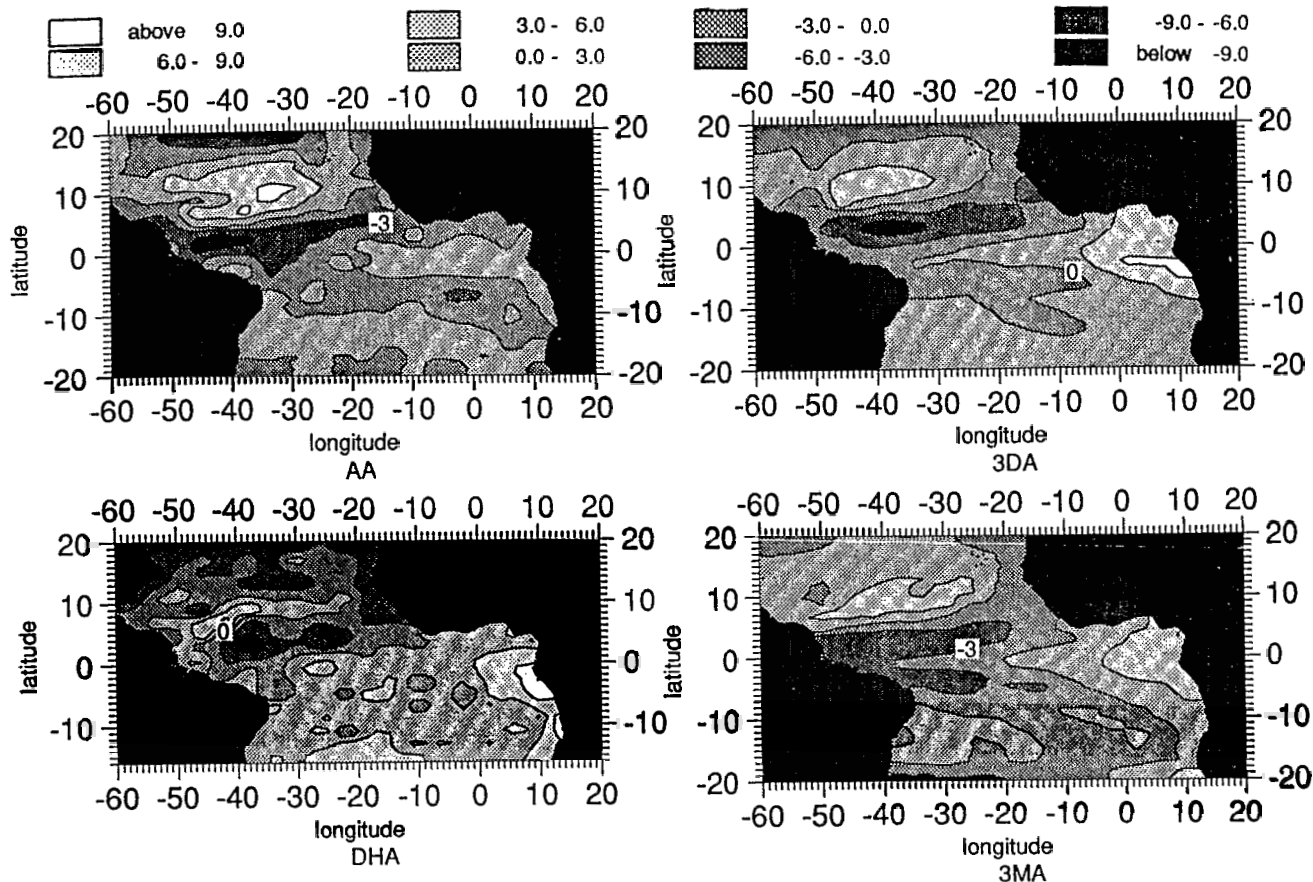
Fig. 1. Dynamic topography anomalies over the tropical Atlantic for a "climatological" March as obtained from the 0/500 dbar in situ dynamic height (DHA in dynamic centimeters), altimetry (AA in centimeters), the linear model 0/500 dbar dynamic height (3MA in dynamic centimeters) and the three-dimensional model 5/500 dbar dynamic height (3DA in dynamic centimeters).
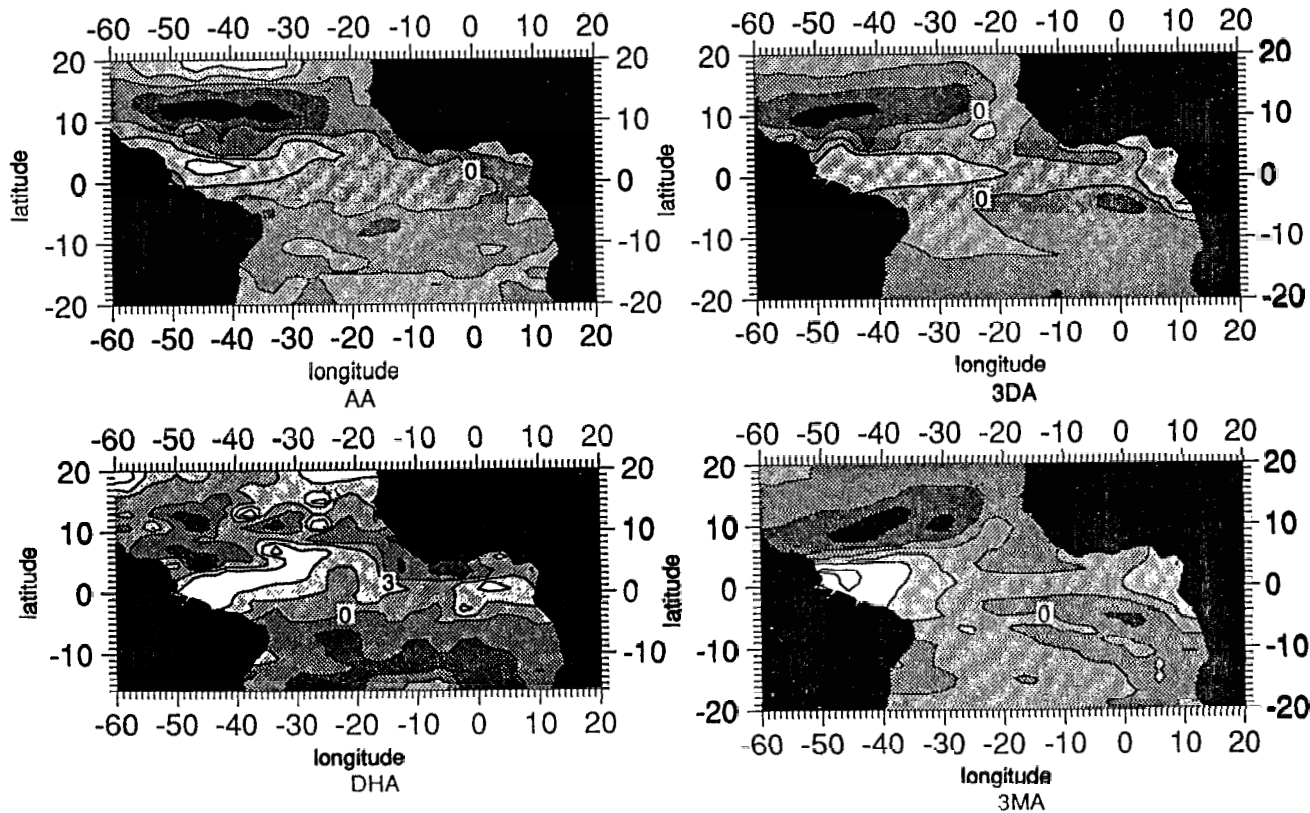
Fig. 2. Same as Figure 1 except for October. Same gray scale as in Figure 1
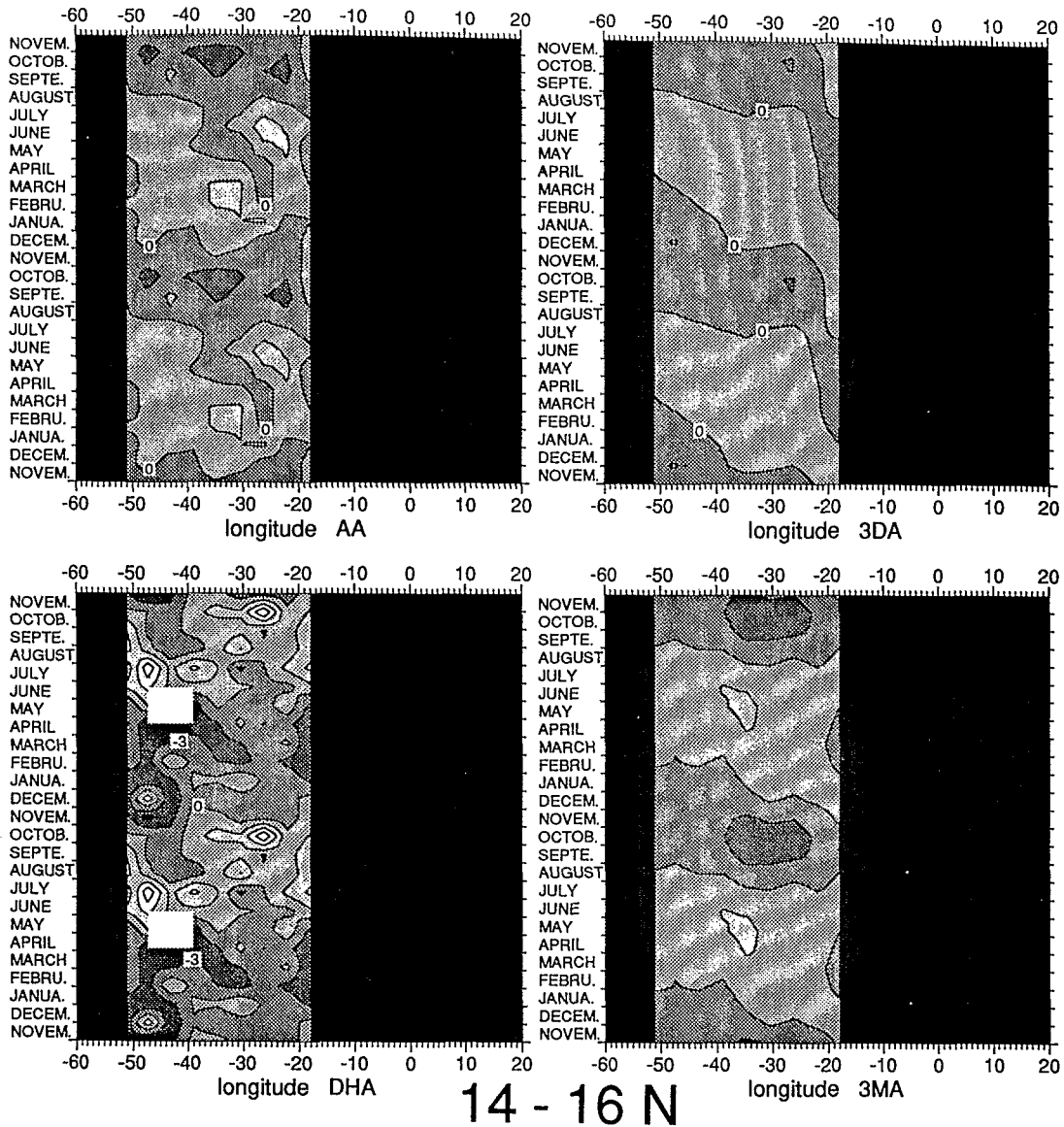
14 - 16 N

Fig. 3.   Seasonal evolution in the North Equatorial Current region (14°–16°N) for the 0/500 dbar in situ dynamic height anomalies (DHA in dynamic centimeters), the altimetric anomalies (AA centimeters), the linear model 0/500 dbar dynamic height anomalies (3MA in dynamic centimeters) and for the three-dimensional model 5/500 dbar dynamic height anomalies (3DA in dynamic centimeters). Same gray scale as in Figure 1.

from 20°N to 20°S) using a cubic spline and a second-degree polynomial (first-degree for short tracks). After adding the mean polynomial over the different cycles to each adjusted profile, the mean profile is then calculated and subtracted. Mean profiles computed over less than seven cycles (or with an inhomogeneous time repartition) are thought to be meaningless and are discarded. The sea level anomalies are adjusted again to absorb long-wavelength errors. A final smoothing is performed using a filter over 180 km. No serious gap in the data has been detected during this analysis. This along-track analysis is then extrapolated into three-dimensional time-space analysis using an objective analysis [De Mey and Robinson, 1987]. The objective analysis algorithm was derived from an analytical correlation function described by

$$f = [1 + R(1 + R/3)][\exp(-R)][\exp(-t^2/rct^2)]$$

with $R = cste*r/rcx$, where r is the distance and t is the time separating the interpolated point and any point in the influence radii areas. On the basis of earlier studies [Cane, 1979; Merle and Arnault, 1985; Reverdin and du Penhoat, 1987; Richardson and Reverdin, 1987], values of 500 km and

TABLE 1a.   Mean rms Computed Over the Climatological Year for Different Areas

	rms, cm			
	AA	3DA	3MA	DHA
NEC	1.9	0.8	1.3	3.0
NECC	2.5	3.2	2.9	5.2
SEC	2.2	3.1	3.5	4.2
SECC	1.8	2.6	2.7	3.7

See Figures 3–6.

TABLE 1b.   Differences of rms Computed Over the Climatological Year for Different Areas

	rms Differences, cm					
	AA/3DA	AA/3MA	3DA/3MA	AA/DHA	3DA/DHA	3MA/DHA
NEC	2.1	2.7	1.1	3.0	3.2	3.9
NECC	2.7	2.9	2.4	4.6	4.2	3.9
SEC	2.6	3.1	1.4	4.3	3.3	3.5
SECC	2.8	2.7	1.5	3.9	3.4	4.0

See Figures 3–6.

140 days were chosen for space and time decorrelation scales rcx and rct. The influence radii which fix the space-time size of the interpolation domain are 300 km and 30 days. The mesh size is 4° in longitude by 2° in latitude. Synoptic maps of altimetric sea level anomaly, each at 3-day intervals from November 1986 to November 1988, were produced. The relative error calculated by the objective analysis varies between 20 and 25%. Monthly averages of these sea level anomalies from November 1986 to November 1988 were then computed.

In situ data.   We also used for our comparison 0/500 dbar dynamic heights (DH). An historical (NANSEN) data set of 20,000 temperature-salinity profiles plus an historical NANSEN-BT data set of 140,000 temperature profiles were used. The DH was computed through a mean T-S relation. The detailed description of the DH computation using temperature profiles and a T-S relationship to supplement hydrographic data has been given by *Merle and Arnault* [1985]. The total error on the monthly 0/500 dbar DH with a 4° in longitude by 2° in latitude gridding is about 2 dynamic

4 - 6 N

Fig. 4.   Same as Figure 3 except for the North Equatorial Countercurrent region (4°–6°N). Same gray scale as in Figure 1.
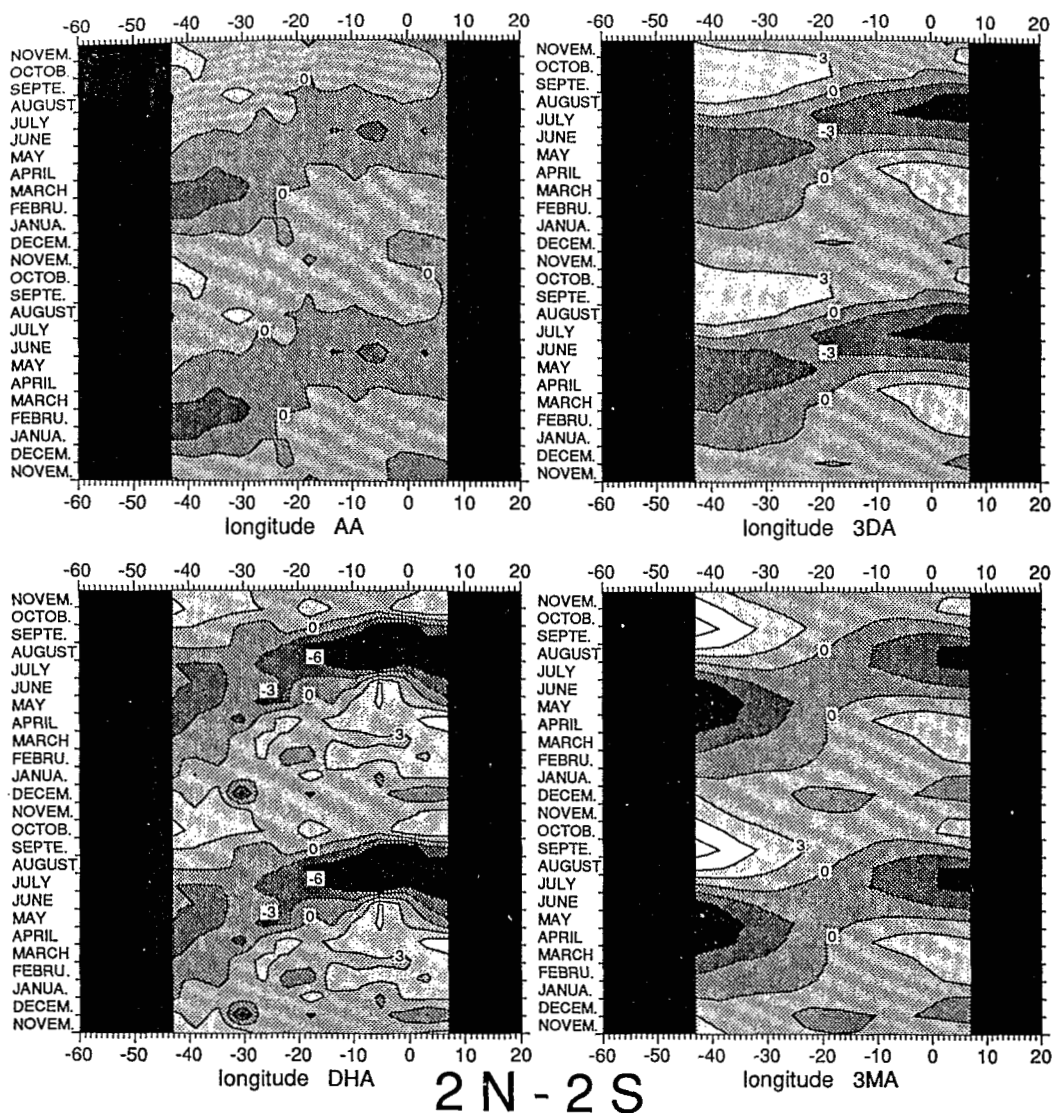
Fig. 5.   Same as Figure 3 except for the South Equatorial Current region (2°N–2°S). Same gray scale as in Figure 1.

centimeters. DH anomalies are computed with reference to the annual mean.

The Models

Linear model.   The first model we used here is a simple one. It computes the linear response of the tropical Atlantic Ocean to the wind forcing through three baroclinic modes. *du Penhoat and Tréguier* [1985] have shown that 95% of the signal obtained with nine modes is provided by the first three. More recently, *du Penhoat and Gouriou* [1987] demonstrated the ability for this kind of model to reproduce DH topography interannual events and at a much lower cost than three-dimensional primitive equation models. They captured quite well the 1983–1984 contrast in the tropical Atlantic Ocean which was the result of an abnormal warm event in 1984 characterized by a huge change of the zonal equatorial DH slope. The decomposition in vertical modes is obtained from a mean density profile, characteristic of the midequa- Atlantic Ocean (24°W). The phase speeds associated

with the first three modes are 2.18, 1.32, and 0.89 m s^{-1}, respectively. These linearized equations are discretized on a staggered grid (Arakawa type C), defined by trigonometric functions so that a variable grid spacing, depending on the area of interest, is obtained. The basin extends from 20°N to 20°S in latitude and from 60°W to 13°E in longitude. In longitude the smallest mesh size (50 km) is near the African and the American coasts. It increases to 115 km in the center of the basin. In latitude the smallest mesh size is at the equator (50 km) to correctly resolve the equatorial radius of deformation. At the northern and southern boundaries the mesh size is 85 km. No-slip boundary conditions have been used on coastal, northern, western, and southern frontiers. The horizontal diffusivity coefficient is 10^3 m^2 s^{-1}. A variable time step (1, 2, and 4 hours for the first, second, and third mode, respectively) is incorporated for the time integration of the model. The model is spun up over 17 years by the climatological *Hellerman and Rosenstein* [1983] wind stress, then run with 1985–1988 monthly wind stress [*Servain*
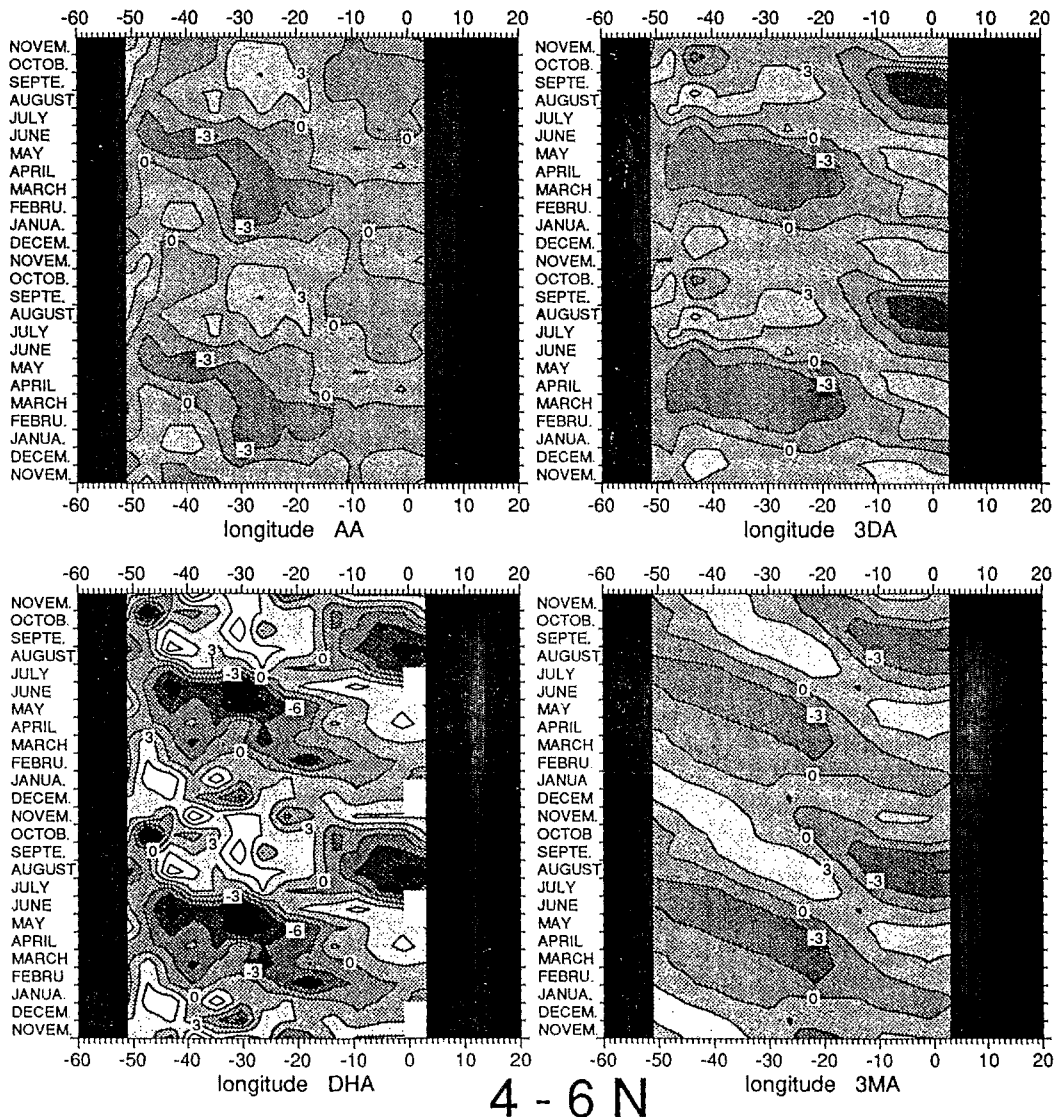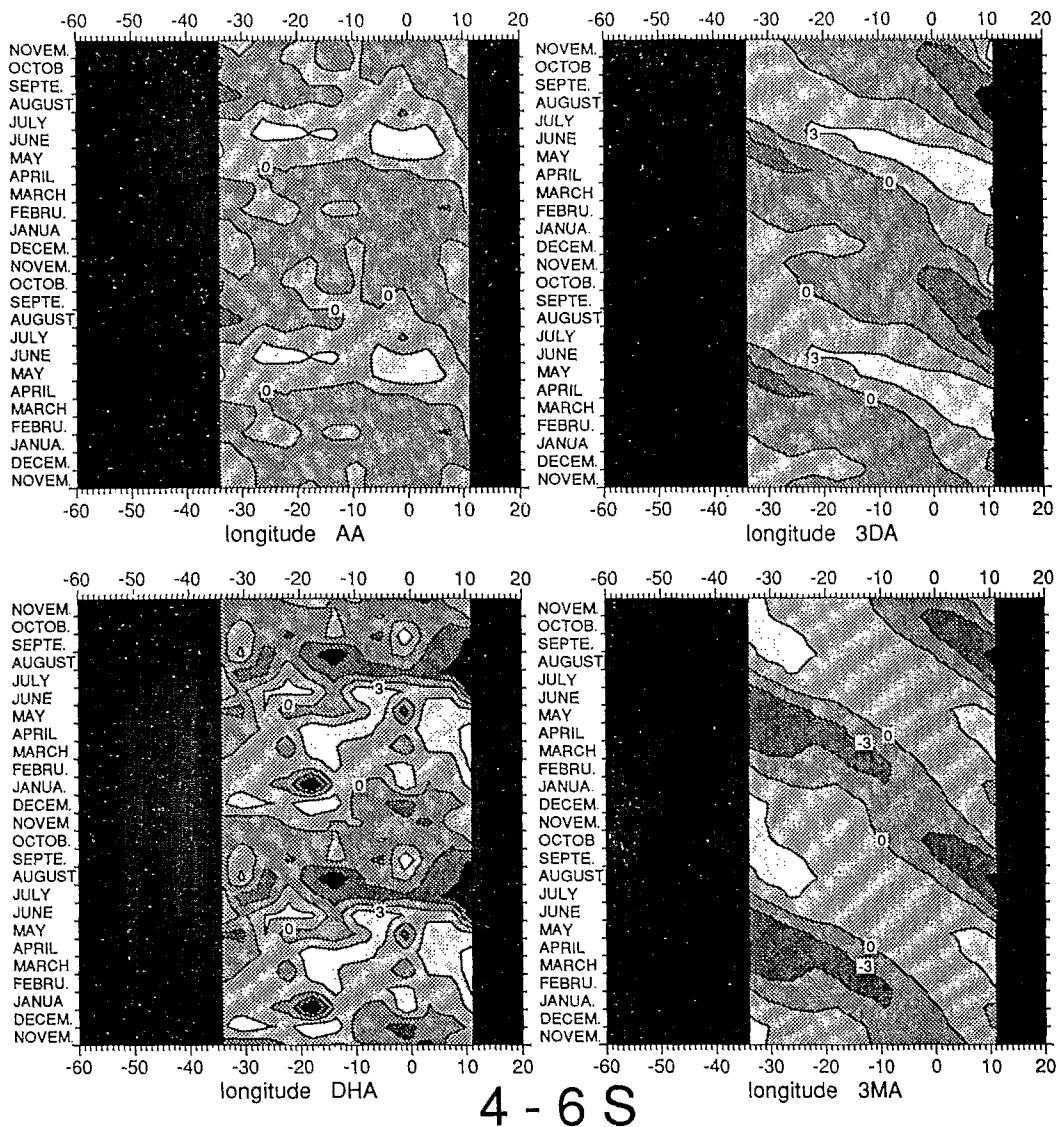
Fig. 6. Same as Figure 3 except for the South Equatorial Countercurrent region (4°–6 S). Same gray scale as in Figure 1.

et al., 1987]. Servain et al.'s original data are converted into wind stress using *Large and Pond's* [1981] formulation. The model is perfectly equilibrated when the 0/500 dbar DH is first computed from the pressure field, and the DH anomaly is then obtained using the DH averaged between November 1986 and November 1988.

Three-dimensional model. The second model we used is a more complex and realistic one. A detailed description of this oceanic general circulation model is presented by *Chartier* [1985] and *Reverdin et al.* [1991]. This model is a multilayer primitive equation model with the Boussinesq, hydrostatic, and rigid lid approximations. The primitive equations are also discretized on a C grid which extends from 50°N to 30°S, from the African to the American coast. The mesh size varies from 0.33° at the equator to 1.5° at the northern and southern frontiers in latitude and from 0.5° near the coasts to 1° at the center of the basin in longitude. There are 17 vertical levels from 0 to 4500 m. In the upper layers the vertical resolution is increased with 13 levels between 0 and 325 m. Neither bottom topography nor islands are

included. No-slip boundary conditions have been used on coastal, northern, western, and southern boundaries, and a buffer zone is imposed at the northern and southern frontiers. The parameterization of vertical diffusivity and viscosity is used by *Philander and Pacanowski* [1981]. They are functions of the Richardson number and vary from the thermal molecular value (1.34×10^{-6} m^2 s^{-1}) up to a maximum of 10^{-2} m^2 s^{-1} when the Richardson number is equal to zero. The horizontal diffusivity is 10^3 m^2 s^{-1}. The state equation is a simple one [*Eckart*, 1958], and density inversions are eliminated at each time step by vertical adjustment to stability of the unstable piece of profile. The external forcing consists of heat fluxes at the air-sea interface and wind stresses. The radiative balance of the shortwaves and the longwaves is obtained from the *Esbensen and Kushnir* [1981] monthly climatology. The sensible and latent heat fluxes are calculated using classical bulk formulas where the air temperature is from the monthly climatology given by *Esbensen and Kushnir* [1981], and the sea surface temperature is issued from the model simulation. The hu-
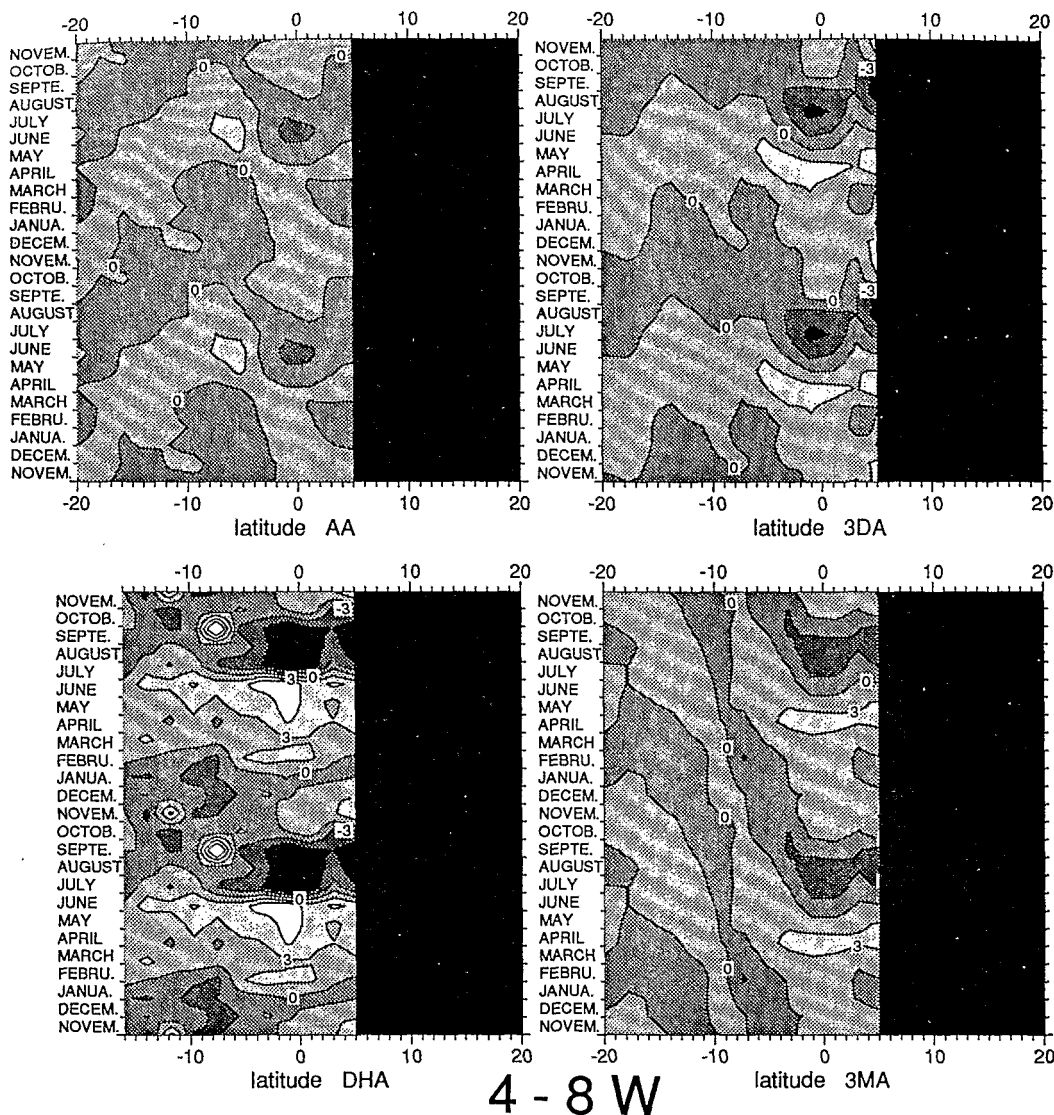
Fig. 7. Seasonal evolution along 4°–8°W for the 0/500 dbar in situ dynamic height anomalies (DHA in dynamic centimeters), the altimetric anomalies (AA in centimeters), the linear model 0/500 dbar dynamic height anomalies (3MA in dynamic centimeters) and for the three-dimensional model 5/500 dbar dynamic height anomalies (3DA in dynamic centimeters). Same gray scale as in Figure 1.

midity is constant and equal to 0.8. The wind stress fields are from *Servain et al.* [1987] as for the linear model. The time step of the model is 1 hour, and during the integration a relaxation toward the *Levitus* [1982] monthly climatology for temperature has been added. These dampings minimize the north and south effects of the closed boundaries by allowing a mass and heat climatology flux at the boundary's neighborhood. Moreover, the surface salinity is damped to the Levitus seasonal climatology in order to allow for the lack of knowledge on the evaporation-precipitation balance. Initially, the ocean is taken at rest, its temperature and salinity being those of the Levitus climatology (monthly for temperature and seasonal for salinity). The model was first forced during 1 year with an annual average wind (calculated on the 1982–1984 period), then during 2 years with a monthly average wind. The simulation was continued using the monthly wind from January 1982 to December 1988. The 5/500 dbar DH is first computed from the simulated temperature and salinity fields using the *Millero and Poisson* [1981]

state equation, and the DH anomaly is then obtained using the DH averaged between November 1986 and November 1988.

3. SEASONAL VARIABILITY

Both the modeled DH and the altimetric signal present the November 1986 to November 1988 variability. As we want to examine the seasonal variability, we recomposed a mean year signal from the 1986–1988 data sets to produce 2-year average monthly maps. We are going to show, on this seasonal basis, which quantities compare the most favorably and what the major discrepancies are.

Basinwide Description

We will not fully describe here the seasonal cycle of the dynamic topography in the tropical Atlantic Ocean, as it has already been done in the past [*Katz*, 1981; *Merle and Arnault*, 1985]. Just a reminder, the dynamic topography in the tropical Atlantic is the superposition of an east-to-west

Fig. 8. Same as Figure 7 except for 24°–28°W. Same gray scale as in Figure 1.

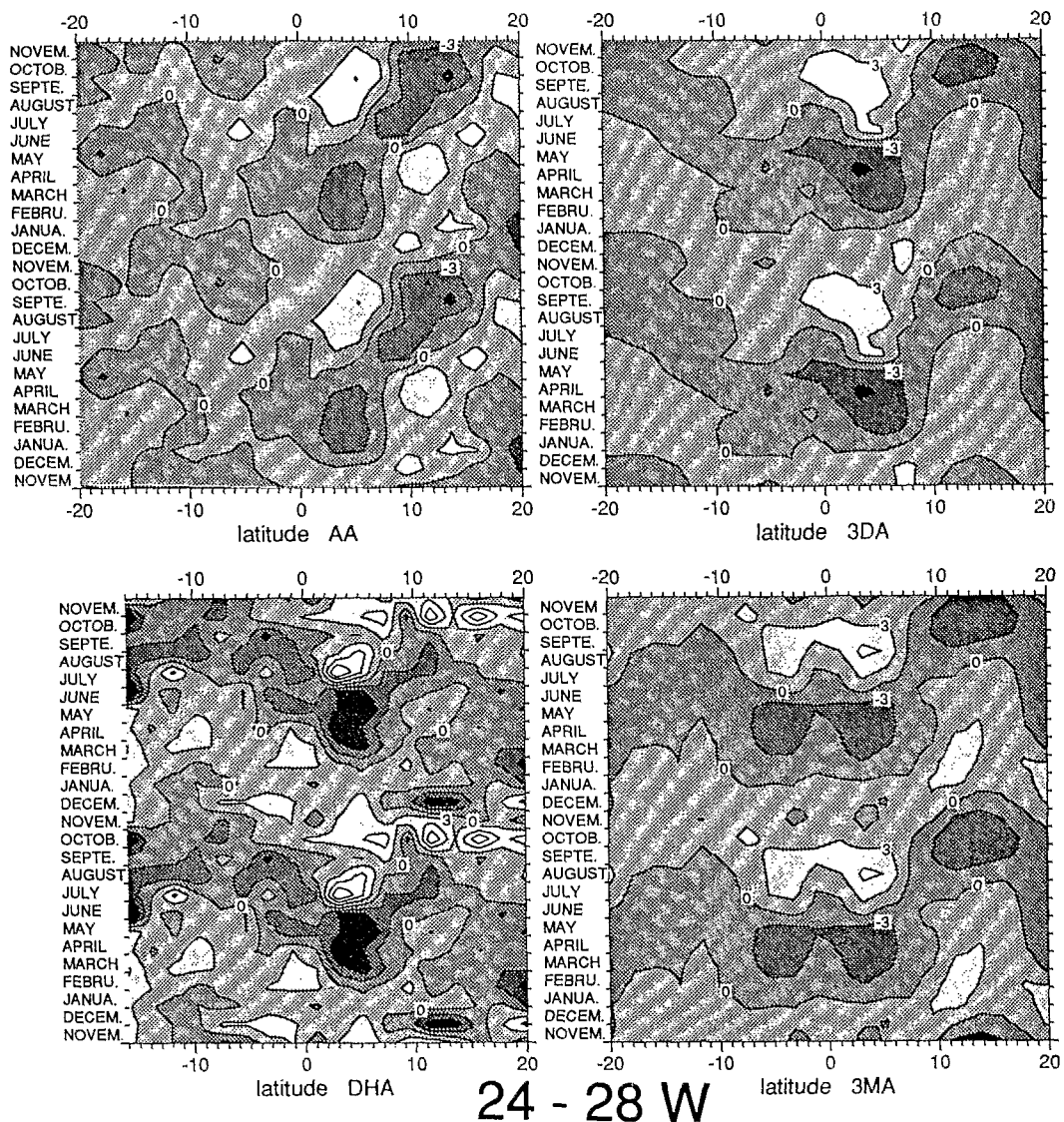rise and a series of zonal ridges and troughs. During the boreal winter-spring season this topography is amorphous in contrast to the summer-fall season when the northern high (2°–3°N) bordering the North Equatorial Countercurrent (NECC) to the south and the equatorial low (0°–2°S) in the center of the South Equatorial Current (SEC) are well formed. For sea level or DH anomalies the seasonal evolution of highs and lows described above results in large zonal patterns of alternatively positive values (when the DH is higher than the annual mean) and negative values (when it is lower) located on the mean positions of the DH highs and lows (Figures 1 and 2). They fluctuate between ±10 cm from March to October, which are opposite months representative of the seasonal variability. The following abbreviations will be used for the different types of anomalies: AA for the altimetric anomalies, DHA for the climatological DH anomalies, 3DA for the three-dimensional model DH anomalies, 3MA for the three vertical mode linear model DH anomalies.

In March, DHA, AA, 3MA, and 3DA present a similar contrast between the southern and the northern hemispheres (Figure 1). The situation is not well defined in the south

contrary to the north where a large and contrasted succession of negative and positive patches appears. Between 15° and 20°N, there are near-zero or negative values reaching −9 cm for both AA and DHA. Positive values (about 6 cm) follow between 7° and 15°N, but the DHA signal is less extended. Between 0° and 7°N, negative values extend from the American to the African coast. It is more pronounced for 3DA, AA, and DHA (−6.9 cm) than for 3MA. Finally, in the eastern part of the Gulf of Guinea a positive structure develops from the African coast toward the west along the equator, hardly standing out for AA (around 0–3 cm) but reaching 6–9 cm in the model results and hydrography.

In October the same north-south difference persists (Figure 2). The northern positive/negative patches described above are identically located, but they have changed sign. As a strong positive anomaly on a dynamic high location and a strong negative anomaly on a dynamic trough location indicate a maximal meridional DH gradient, the geostrophic zonal currents, which are proportional to the meridional DH gradients, are therefore stronger during this period than during the boreal spring.
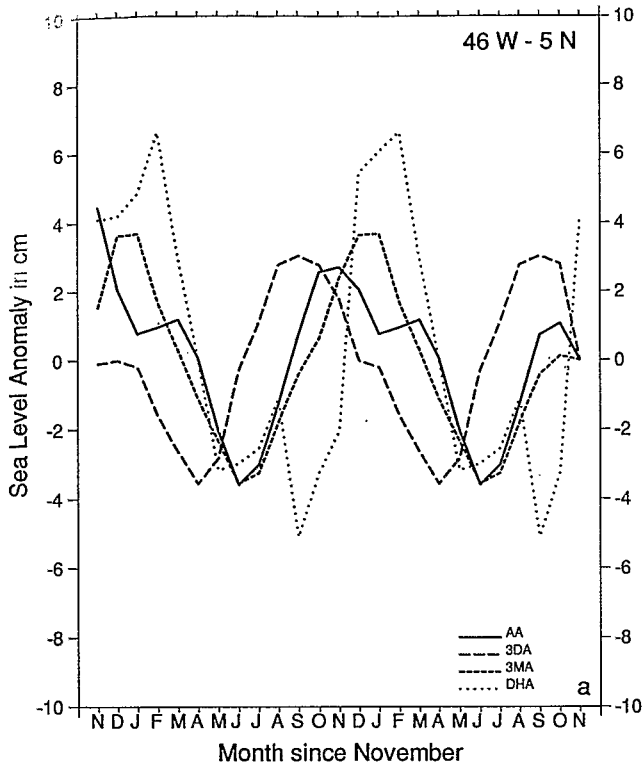
Fig. 9a. Comparison of the seasonal cycle at 46°W–5°N of the in situ dynamic height anomalies (AA, solid line) (in centimeters) the linear model 0/500 dbar dynamic height anomalies (3MA, short dashed line) (in dynamic centimeters), three-dimensional model 5/500 dbar dynamic height anomalies (3DA, long dashed line) (in dynamic centimeters). A running mean over 3 months is performed in order to eliminate small-scale noise.
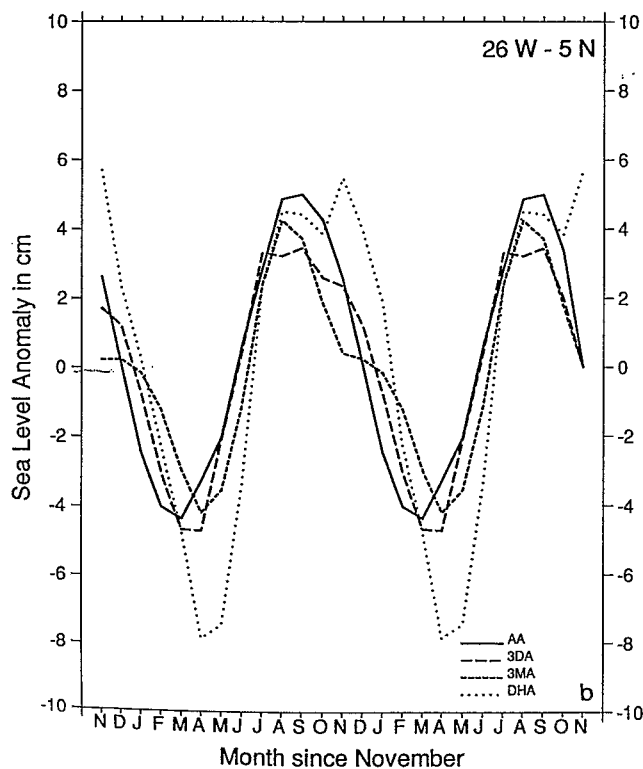
Seasonal Longitudinal and Latitudinal Evolution

To show more efficiently the wave propagation phenomenon or the time shifting in the seasonal variability of the data, we also looked at the seasonal evolution of the dynamic structures along the latitudes of the main current cores, 14°–16°N for the North Equatorial Current (NEC), 4°–6°N for the NECC, 2°N–2°S for the SEC, 4°–6°S for the South Equatorial Countercurrent (SECC), and along two meridians located in the center of the basin (28°W) and in the Gulf of Guinea (4°W).

Seasonal longitudinal evolution in the NEC region. For the northernmost region (14°–16°N) both AA and DHA (Figure 3) present more variability with smaller-scale structures than the models. The AA, 3DA, and 3MA signal is negative (about −3/6 cm) from August to December, but DHA is time-shifted with negative values from October–November to May. At 20°W, 3MA and AA present a second negative extremum along the African coast in the spring after the one in the fall. This can be related to the local upwelling off Dakar. A westward propagation is also evidenced by a time lag correlation matrix analysis for AA, 3DA, and 3MA. However, it seems a little bit faster for AA (about 0.70 m s^{-1}) than for the models (0.35 for 3DA and 0.45 m s^{-1} for 3MA). The mean annual rms differences computed for this region are given in Table 1. Except for the AA/3MA comparison (2.7 cm) which is larger than the rms for AA (1.9 cm) or 3MA (1.3 cm), these rms differences are generally of the same order as the rms of the products alone.

Seasonal longitudinal evolution in the NECC region. Farther south, in the NECC region, DHA still present smaller spatial structures of larger amplitude (about 20 cm) (Figure 4). West of 15°W, every product evidences a nega-

Fig. 9b. Same as Figure 9a, except for 26°W–5°N.

Fig. 9c. Same as Figure 9a, except for 2°W–5°N.

Fig. 10a. Same as Figure 9, except for 46°W–1°N.

tive patch of −3/6 cm from February to July. This signal reaches more than −9 cm for DHA. A particularly good agreement exists between 3DA and the AA west of 25°W. In the east (15°W–3°E) the negative AA signal is hardly outlined
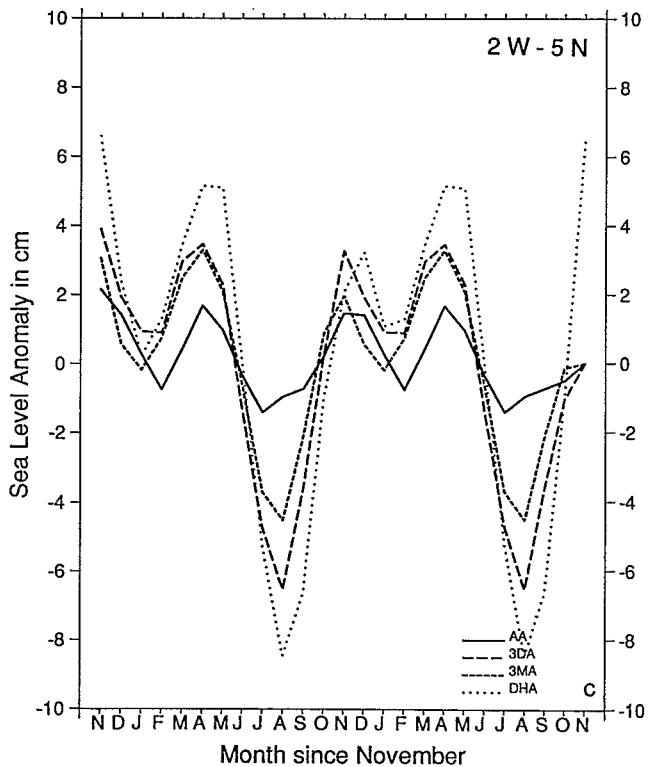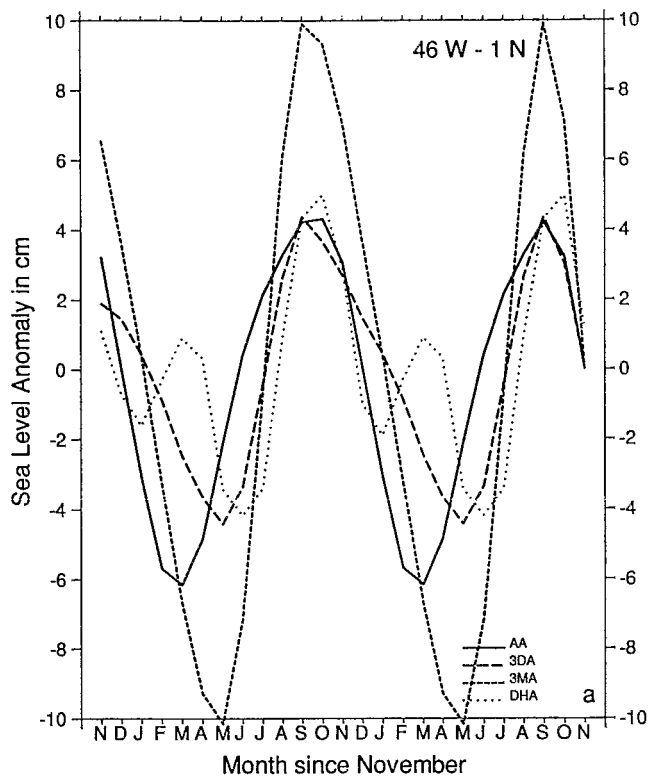
(−3 cm); otherwise it reaches less than −9 cm for DHA and 3DA and −6 cm for 3MA. However, the semiannual signal, characteristic of the tropical Atlantic eastern basin, is reproduced by AA in July–September, then January–March. The four pictures also clearly show a westward propagation during spring-summer. The phase velocity varies from about 0.40 m s^{-1} for 3MA to 0.50–0.60 m s^{-1} for AA, 3DA, and DHA. According to the linear waves theory the velocity for the first meridional mode Rossby wave is equal to $C/3$, where C is the Kelvin wave phase speed. This phase speed for a second vertical mode Kelvin wave ranges from 1.10 to 1.50 m s^{-1} in the tropical Atlantic. The velocities obtained above could be therefore the signal of a second vertical/first meridional mode Rossby wave. The NECC region, a region of large variability, is also one of the areas where the comparison between the four quantities gives the best results as shown in Table 1.

Seasonal longitudinal evolution in the SEC region. Along the equator (Figure 5) the main disagreement between AA and DHA, 3DA, or 3MA is due to the relative weakness of the AA signal in the eastern part of the Gulf of Guinea. A clear separation of the basin in an eastern (east of 15°–20°W) and a western part (west of 15°–20°W) is shown by AA, 3DA, and 3MA. In the west the annual signal is dominant with negative values between March and May and positive values between July and February. In the east the signal presents two negative extrema (April–August and December–January) and two positive ones (January–May and September–November), but the amplitude of the AA signal is about 6/9 cm instead of 12/20 cm for the other quantities. Following the wave theory, one would expect to see an eastward propagation with a 1.10/1.50 m s^{-1} phase speed as anticipation of the Rossby wave at 5°N, but such a propagation is not clear in Figure 5.
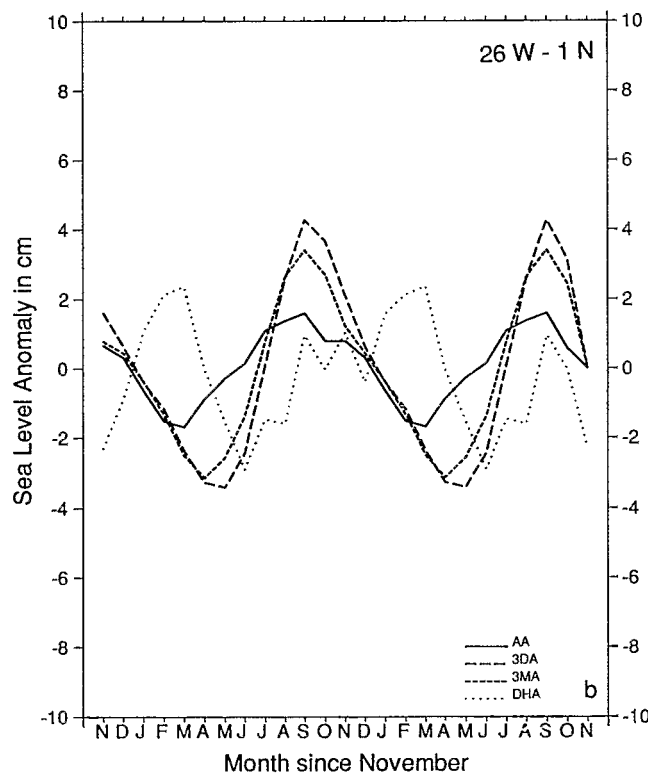
Fig. 10b. Same as Figure 9, except for 26°W–1°N.
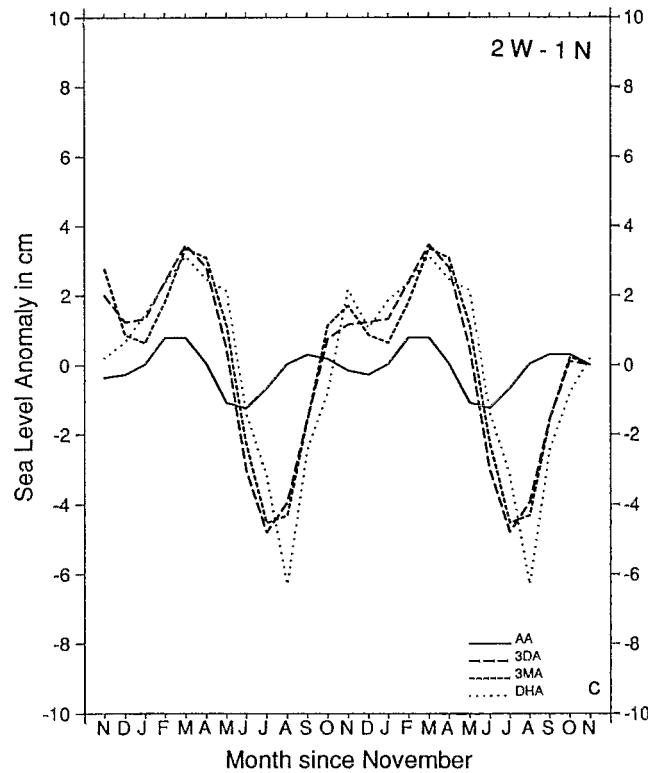
Fig. 10c. Same as Figure 9, except for 2°W–1°N.

ANNUAL AMPLITUDE
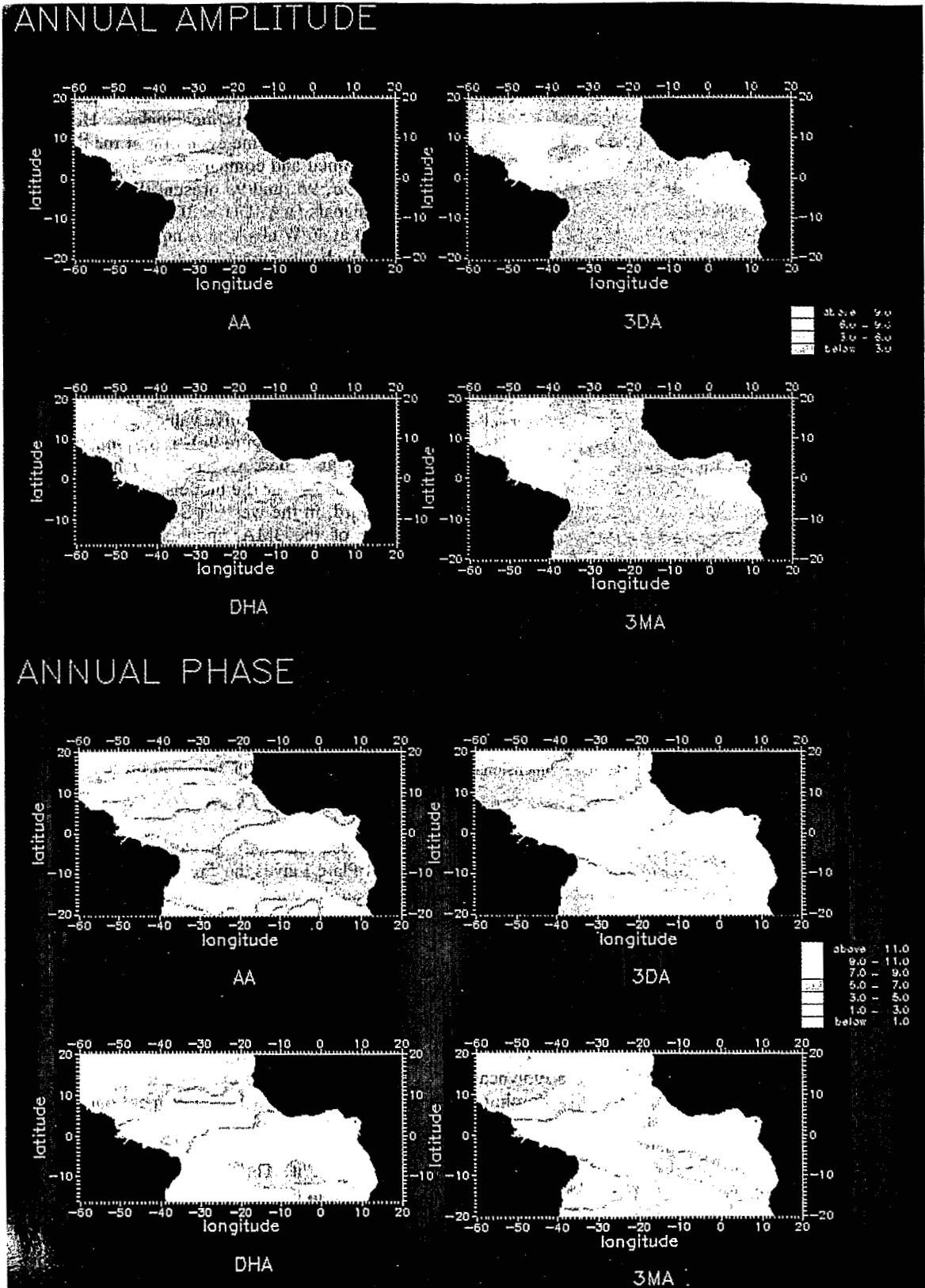
ANNUAL PHASE

Plate 1. Annual amplitude (in dynamic centimeters or in centimeters) and phase (in months) as computed from a cosine function fit of the seasonal signal for the 0/500 dbar in situ dynamic height anomalies (DHA), the altimetric anomalies (AA), the linear model 0/500 dbar dynamic height anomalies (3MA), and for the three-dimensional model 5/500 dbar dynamic height anomalies (3DA). Amplitude is shown from below 3 cm (red) to above 9 cm (light yellow).

CLIMATOLOGY
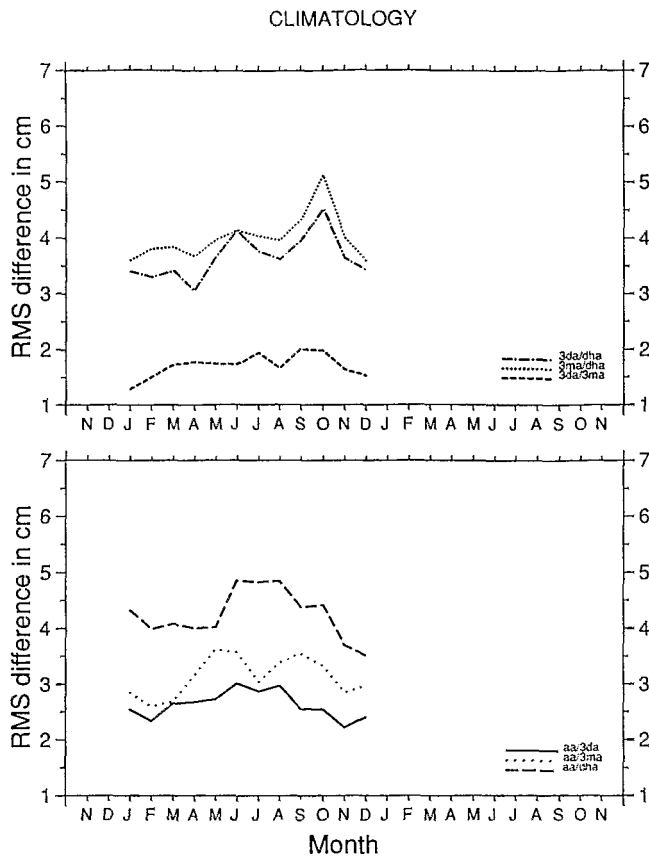
Fig. 11.   Mean rms differences in centimeters between altimetry and in situ dynamic height anomalies (solid line), three-dimensional model and dynamic height anomalies (spaced dotted line), linear model and dynamic height anomalies (long dashed line), altimetry and three-dimensional model anomalies (dashed-dotted line), altimetry and linear model anomalies (dotted line), and three-dimensional model and linear model anomalies (dashed line).

Seasonal longitudinal evolution in the SECC region.   The southern hemisphere signal (Figure 6) also clearly shows a westward propagation for the models as in the NECC region. A time lag correlation matrix gives a propagation velocity around 0.35 m s^{-1}. However, this propagation is not so evident for both the data, AA or DHA. It seems therefore that both models emphasize the wave propagation phenomenon in the southern hemisphere. The signal is negative from August to April for AA, and from July to December for DHA. For the models the negative values begin in June near the African coast and reach the American coast in March. In the east a very slight secondary negative extremum can be seen in January for AA and the models but not for DHA.

Seasonal latitudinal evolution in the Gulf of Guinea along 4°W and in the center of the basin at 28°W.   The qualitative agreement especially between AA and 3DA is also evidenced looking at the signal south of Abidjan, along 4°W (Figure 7). Both phase and amplitude look similar and compare much more favorably together than with DHA. AA and 3DA present an inverse V-shaped structure centered along 8°S. The latitudinal limit between the seasonal signal (to the south), and the semiannual signal (stronger toward the African coast) is around 2°N. The evolution along 28°W (Figure 8) also presents a good agreement between AA, 3DA, and 3MA, except that the models emphasize the wave

phenomenon by showing a rather symmetric structure along the equator, especially for 3MA.

Local Comparisons

For such short time series (12 points) the computation of a correlation coefficient is meaningless. However, a more precise view for the time evolution of the different products can be obtained and compared at selected points.

Figures 9a, 9b, and 9c present the seasonal evolution of the four signals (AA, DHA, 3DA, and 3MA) in the NECC core (5°N) at 46°W near the American coast, at 26°W in the center of the basin, and at 2°W near the African coast. In the west (Figure 9a), every signal seems to be time-shifted in comparison with another one. Better agreement is offered by 3MA and AA. The AA, 3DA, and 3MA signal amplitudes are mostly the same, about 8 cm, but the DHA signal amplitudes have larger variations (12 cm). Eastward (Figure 9b), the agreement is very good for both amplitude and phase, even if DHA reach larger negative values (−8 instead of −5 cm) in spring. In the east (Figure 9c), if the timing is relatively the same for all quantities, AA have a much smaller amplitude (4 cm instead of 7–9 for the models and 14 cm for DHA).

Southward, in the western SEC (Figure 10a) at 1°N, the amplitude of the 3MA signal seems unrealistic. This is certainly due to the proximity of the Brazilian coast and the boundary condition effect. DHA also present a semiannual signal which is not reproduced by others. Eastward (Figure 10b and 10c), the weak AA signal is shown once more, and during the upwelling season, a significant time shifting of AA compared with DHA, 3MA, and 3DA (about 2 months) is also shown. It is interesting to note that this absence of altimetric signals in the Gulf of Guinea has already been observed by *Ménard* [1988] using other satellite altimeters, methods, and corrections. We will discuss this point later.

Statistics

We fit these seasonal signals by a cosine function $A \cos (wt + f)$. Plate 1 gives the annual amplitudes and phases. In the west, all the quantities show more than 6-cm variations along 2°–3°N and 10°N, separated by a zone of relative minimum (less than 3 cm) which is more evident for the models and AA than for DHA. These extrema are located a few hundred kilometers off the coast except for 3MA. In the east the amplitude is larger than 3 cm except for AA. Another maximum appears for AA north of 17°N, consistent with the intensification of the annual cycle of winds.

All the annual phases evidence a "pivot" line across the NECC around 5°N, as already mentioned by *Merle and Arnault* [1985]. The annual cycle of DHA or AA reaches its maximum in summer-fall north of the NECC and in winter-spring south of it. This is in agreement with the NECC intensification in the fall when a dynamic high at 2°–3°N and a dynamic low at 8°–10°N appear. However, AA present a uniform phase lag up to 8°N along the northern American coast as observed by *Carton* [1989]. Therefore the region of high phase is well separated from the coast, contrary to DHA or 3MA, especially. Another pivot point is present along the equator, at 20°W for the models, 25°W for AA, and 30°W for DHA. In the Gulf of Guinea the extremum occurs in summer-fall, and in the west it occurs in spring. Finally, north of 15°N, AA also show a phase lag, according to the NEC variation. This lag is only hardly shown by 3DA.
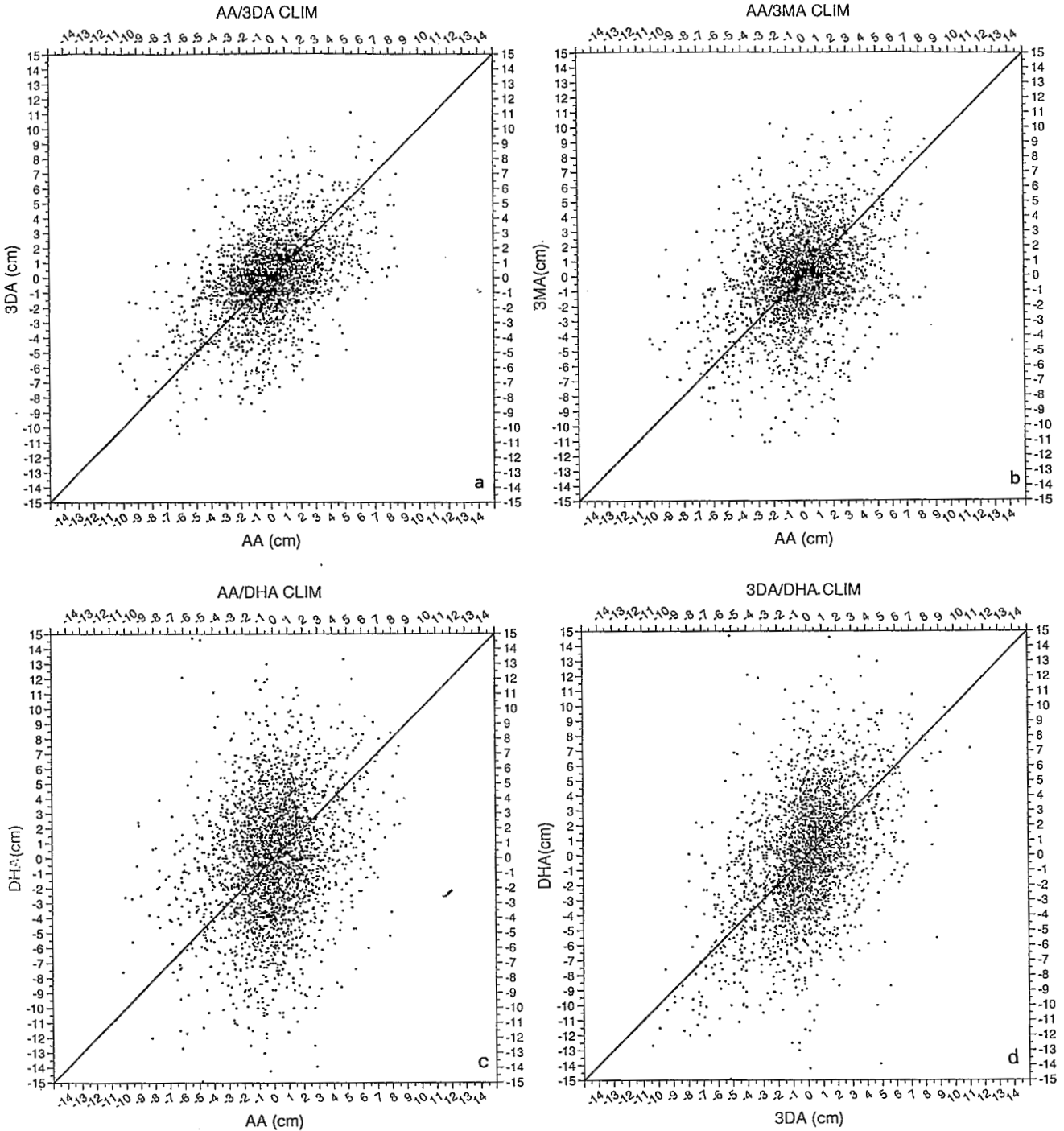
Fig. 12. Scatterplots for the seasonal cycle between (*a*) altimetric anomalies and three-dimensional model results (AA/3DA), (*b*) altimetric anomalies and linear model results (AA/3MA), (*c*) altimetric anomalies and in situ dynamic height anomalies (AA/DHA), (*d*) three-dimensional model results and in situ dynamic height anomalies (3DA/DHA), (*e*) linear model results and in situ dynamic height anomalies (3MA/DHA), and (*f*) three-dimensional model and linear model results (3DA/3MA).

The second harmonic amplitudes (not presented here) are usually less than 6 cm. The same regions of maximal amplitude appear: the northwest region (especially for AA) and the eastern Gulf of Guinea (but weaker for AA).

The seasonal evolution of monthly mean rms differences between all pairs of data over the whole basin is given in Figure 11. Looking first at the comparisons with AA, we see that the largest values are reached by the rms AA/DHA. The

mean rms value is around 4.2 cm. However, the rms of 3DA/DHA and 3MA/DHA, the other 1986–1988 products compared to the DH climatology, are not significantly different with mean values about 3.7 and 4 cm, respectively. The rms differences between AA/DHA peak during boreal summer (4–5 cm). This is during the upwelling in the Gulf of Guinea. On the other hand, both the models, when compared to DHA, present an extremum (around 5 cm) in

3MA/DHA CLIM

3DA/3MA CLIM
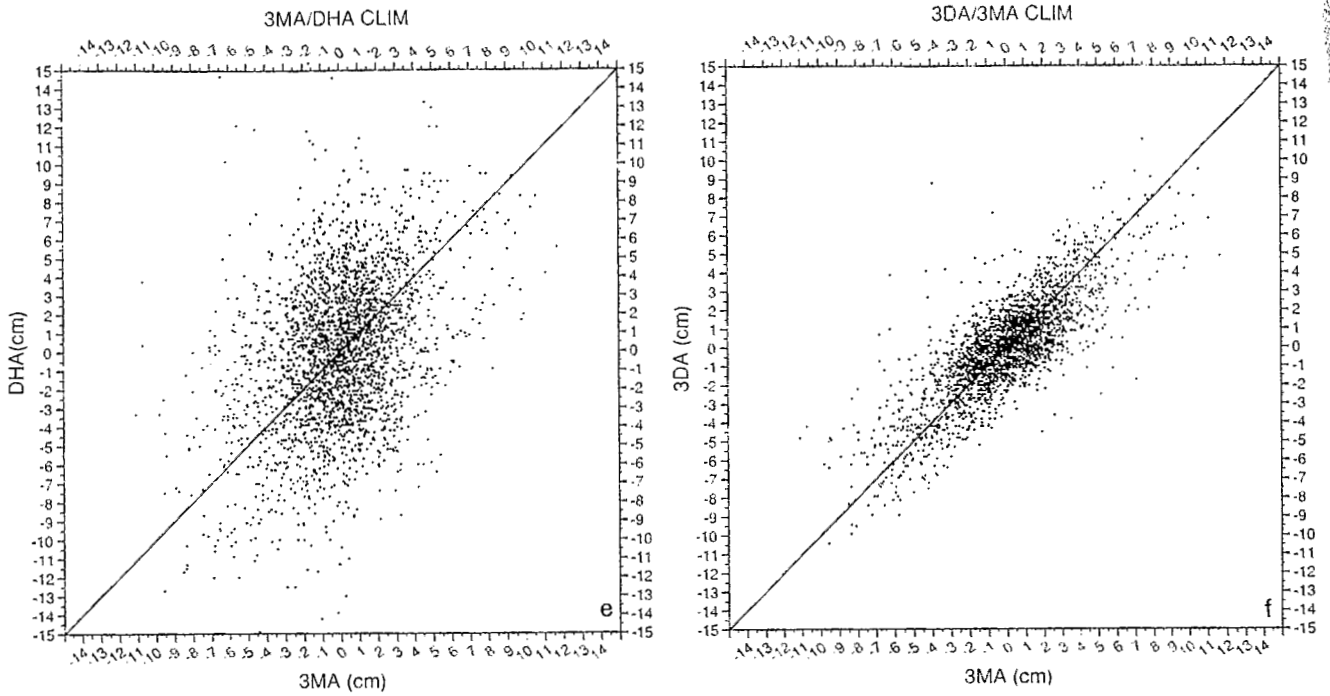
Fig. 12.   (continued)

NOVEMBER 1986
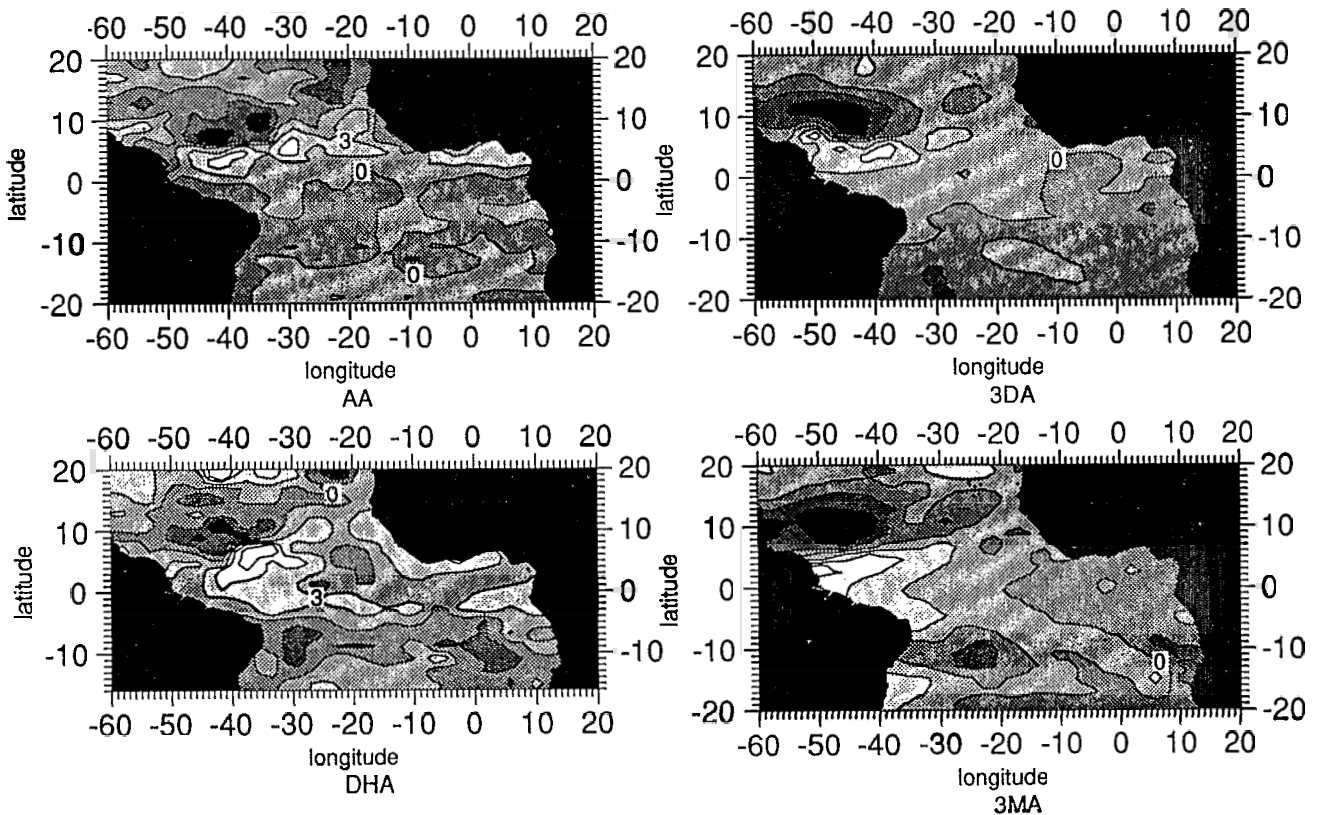
Fig. 13.   Dynamic topography anomalies over the tropical Atlantic for November as obtained from the 0/500 dbar in situ dynamic height (DHA in dynamic centimeters), and for November 1986 as obtained from altimetry (AA in centimeters), the linear model 0/500 dbar dynamic height (3MA in dynamic centimeters) and the three-dimensional model 5/500 dbar dynamic height (3DA in dynamic centimeters). Same gray scale as in Figure 1.

MARCH 1987
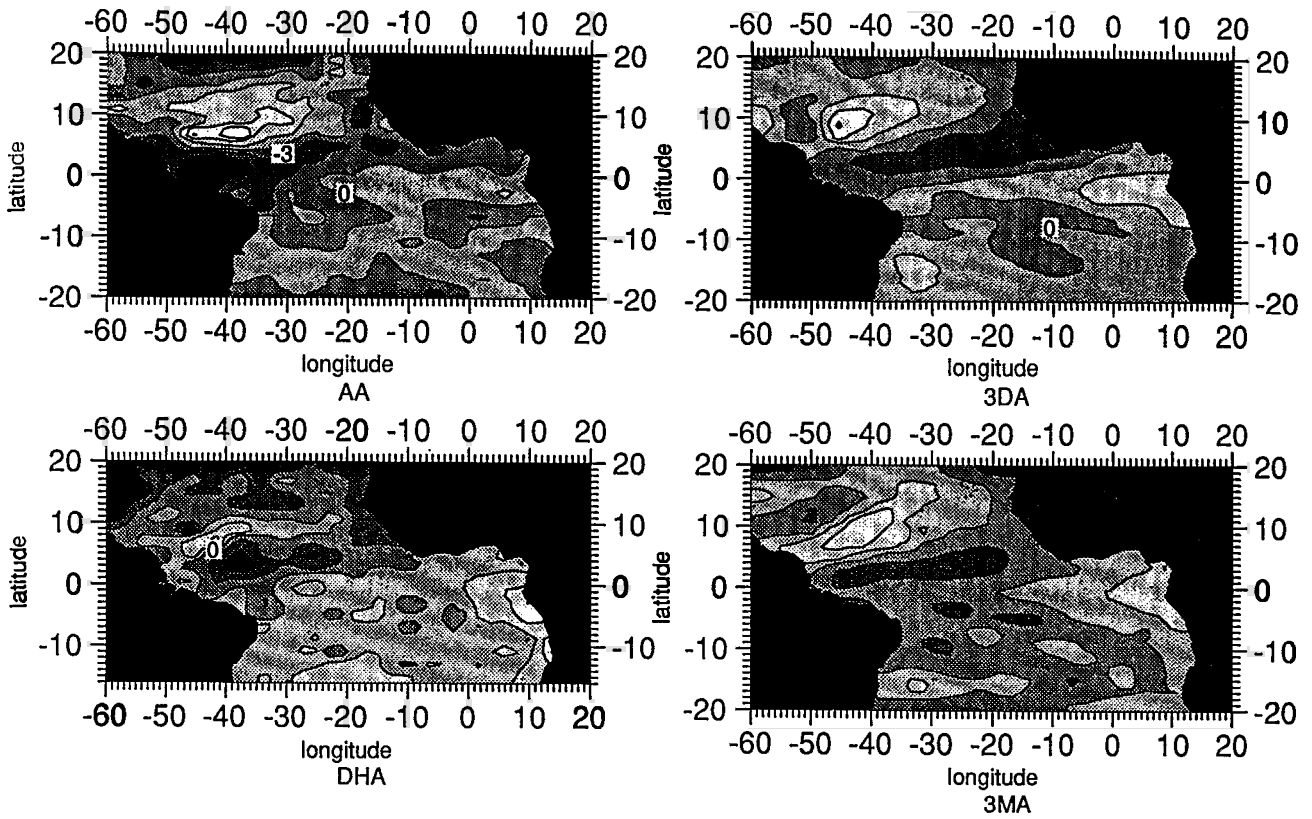
Fig. 14. Same as Figure 13 except for March 1987. Same gray scale as in Figure 1.

JULY 1987
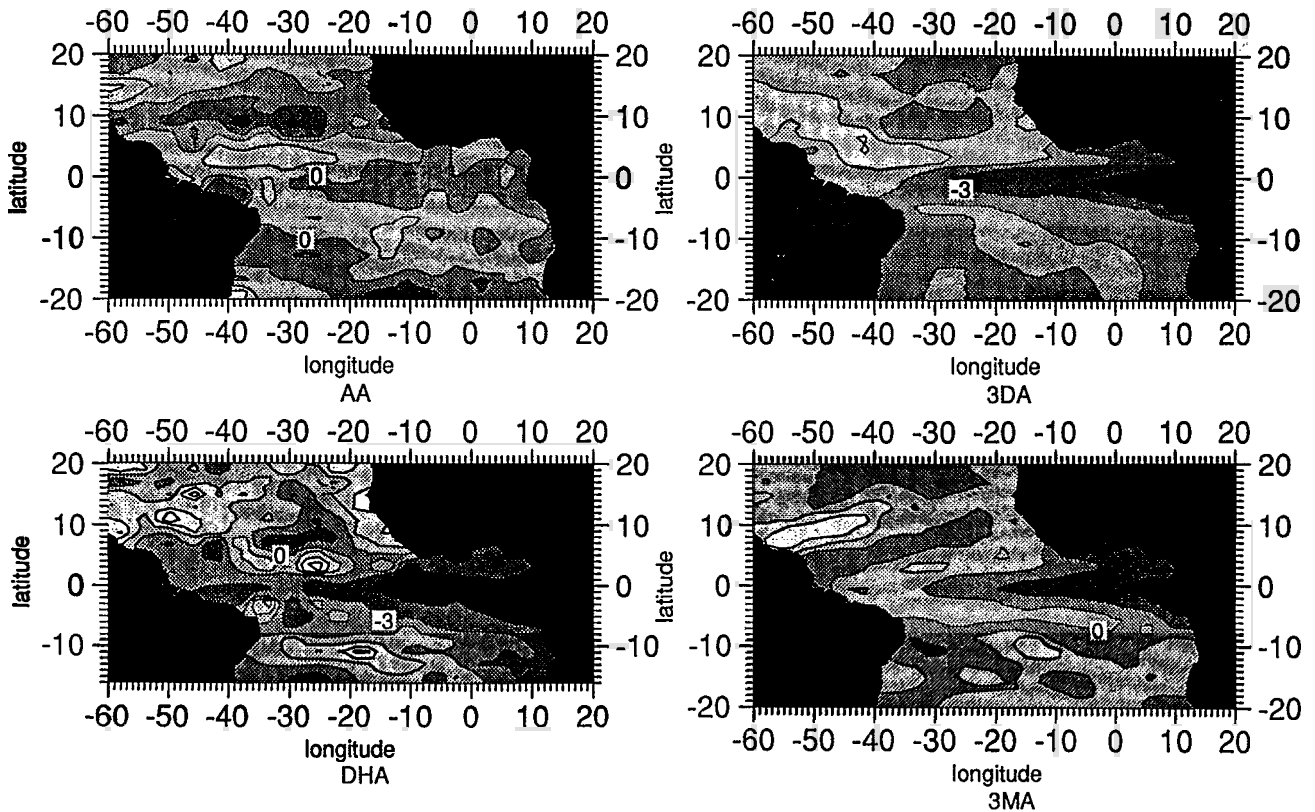
Fig. 15. Same as Figure 13 except for July 1987. Same gray scale as in Figure 1.

OCTOBER 1987
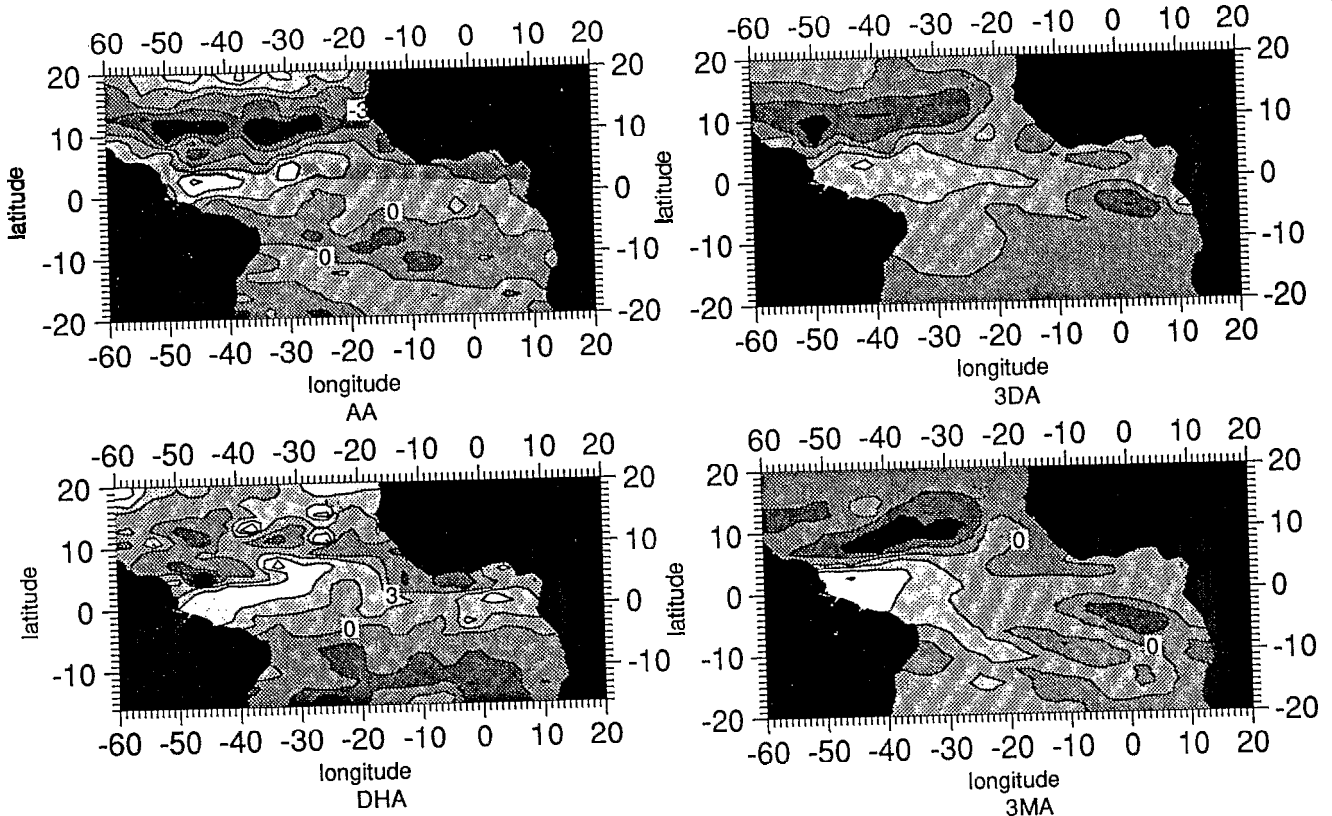
Fig. 16.　Same as Figure 13 except for October 1987. Same gray scale as in Figure 1.

MARCH 1988
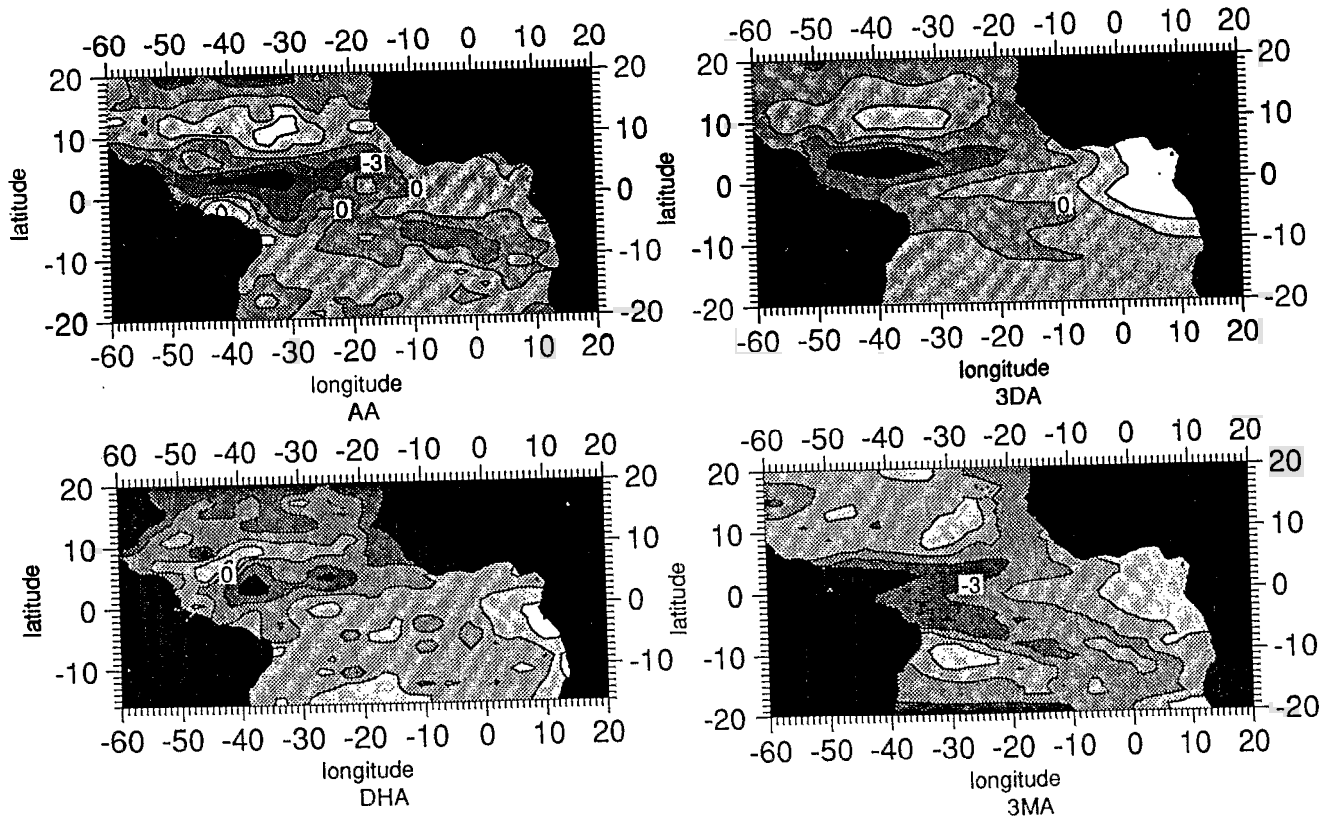
Fig. 17.　Same as Figure 13 except for March 1988. Same gray scale as in Figure 1.

JULY 1988
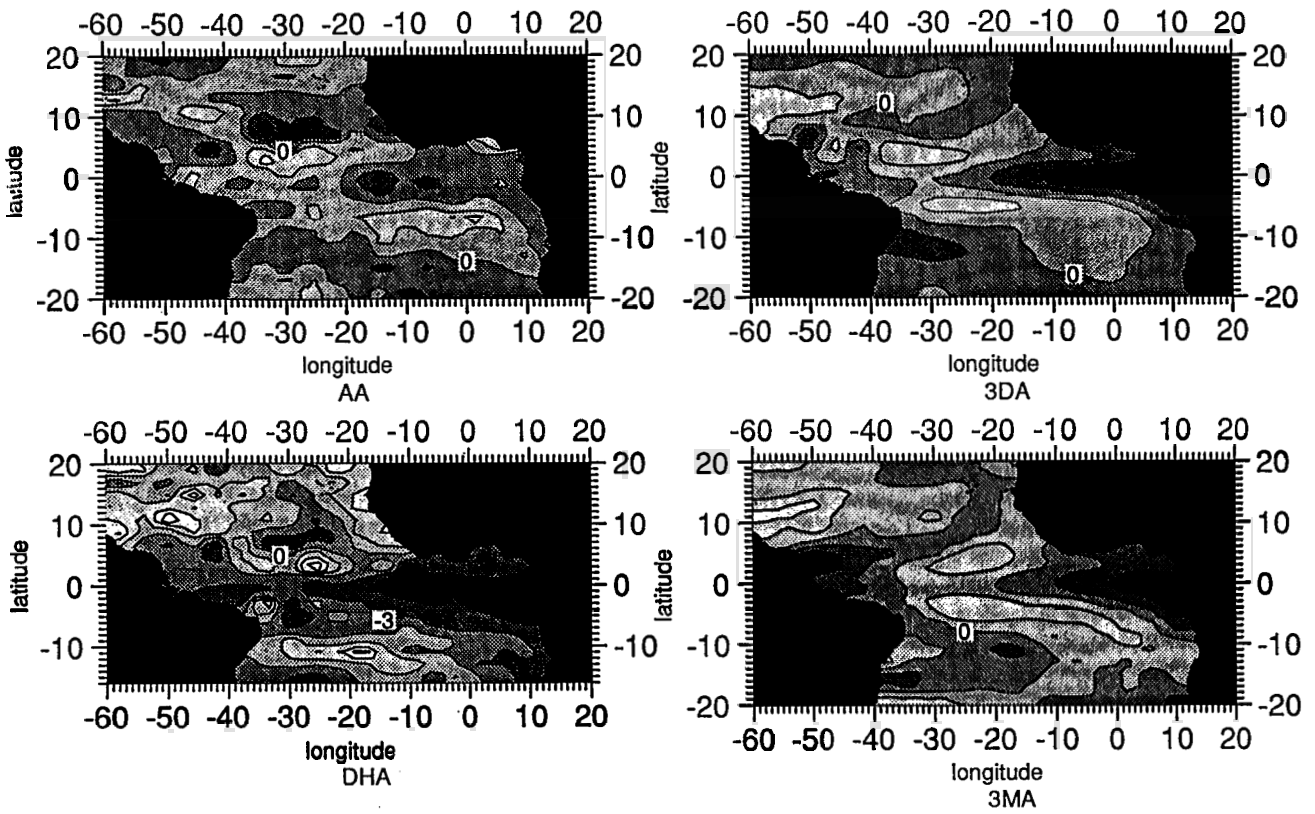
Fig. 18. Same as Figure 13 except for July 1988. Same gray scale as in Figure 1.

OCTOBER 1988
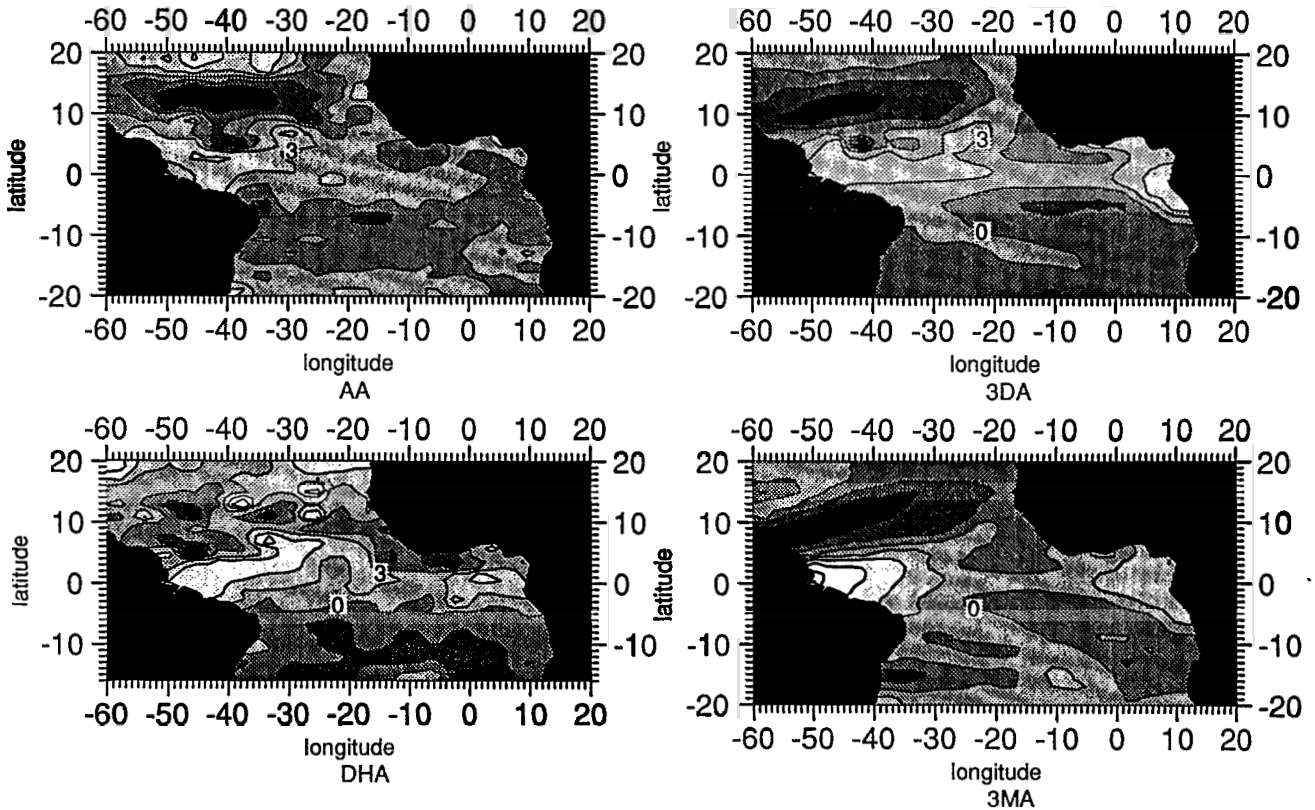
Fig. 19. Same as Figure 13 except for October 1988. Same gray scale as in Figure 1.
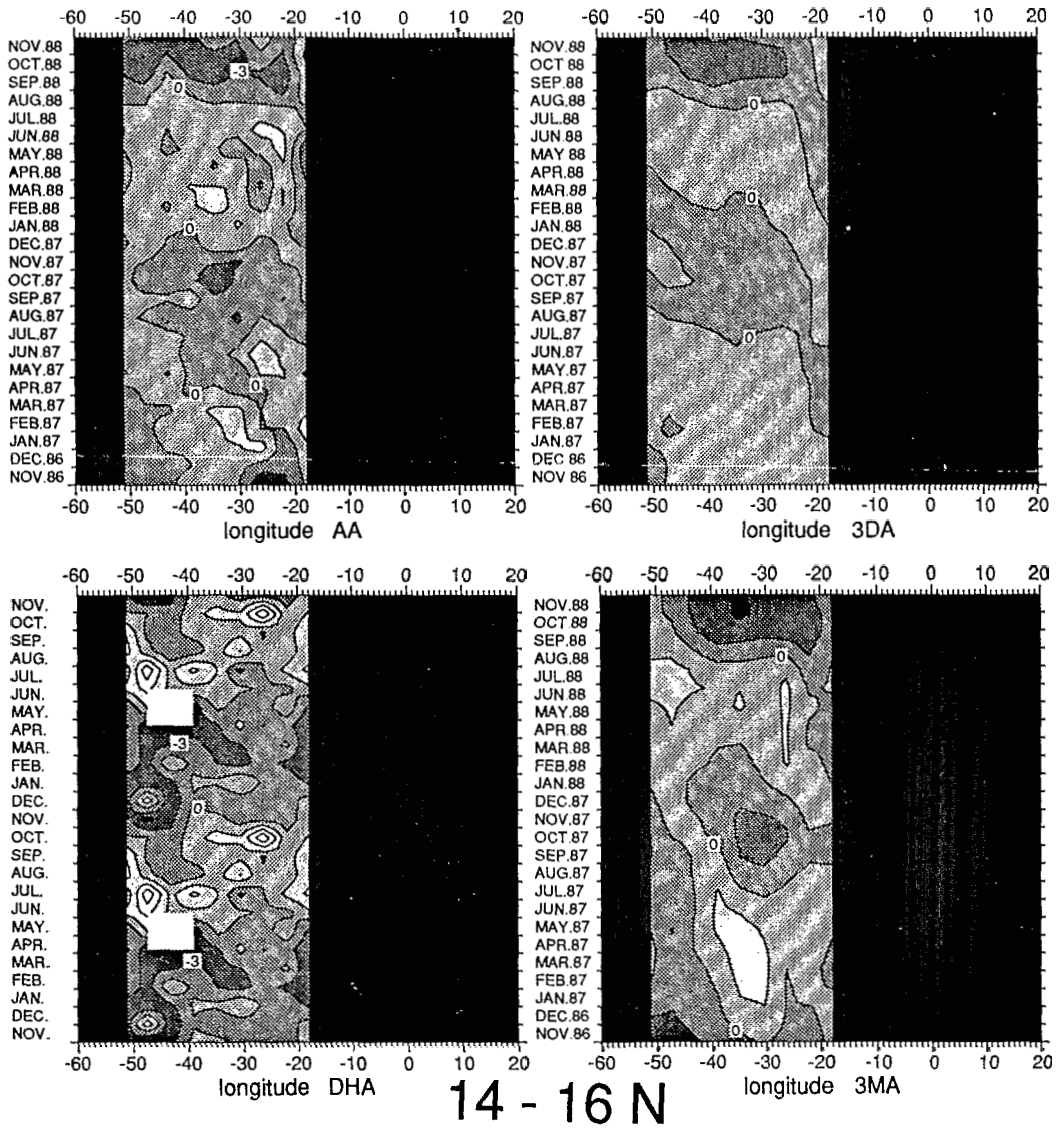
Fig. 20. Seasonal evolution in the North Equatorial Current region (14°–16°N) for the 0/500 dbar in situ dynamic height anomalies (DHA in dynamic centimeters), from November 1986 to November 1988 for the altimetric anomalies (AA in centimeters), the linear model 0/500 dbar dynamic height anomalies (3MA in dynamic centimeters), and for the three-dimensional model 5/500 dbar dynamic height anomalies (3DA in dynamic centimeters). Same gray scale as in Figure 1.

October. This is due to a large negative anomaly extending northward from 10°N in the model results but not in the DHA (see also Table 1). The good agreement between the two models with a mean rms about 1.7 cm is also noteworthy. It emphasizes the ability of such linear models to reproduce the seasonal cycle of an integrated quantity such as DH in the tropics. But the most interesting result is presented by the rms AA/3DA: 2.6 cm as a mean. Thus the best agreement between a model and a data set is obtained with AA and 3DA.

TABLE 2a. Mean rms Computed Between November 1986 and November 1988 for Different Areas

	rms, cm		
	AA	3DA	3MA
NEC	2.3	1.5	2.4
NECC	3.2	3.6	3.1
SEC	2.4	3.1	3.3
SECC	2.0	2.5	2.5

See Figures 20–23.

TABLE 2b. Differences of rms Computed Between November 1986 and November 1988 for Different Areas

	rms Differences, cm		
	AA/3DA	AA/3MA	3DA/3MA
NEC	2.0	2.4	1.7
NECC	3.3	3.3	2.7
SEC	3.1	3.4	1.4
SECC	3.0	3.1	1.6

See Figures 20–23.

Fig. 21. Same as Figure 20 except for the North Equatorial Countercurrent region (4°–6°N). Same gray scale as in Figure 1.

In conclusion, the seasonal cycle of the tropical Atlantic surface topography is rather identically presented by all the data sets and the models. They all show an opposition between the summer/fall season and the winter/spring season, and the Gulf of Guinea is affected by a semiannual signal in all the products, even if the AA signal is too weak. Figure 12a clearly shows the good agreement which exists between AA and 3DA. No significant bias from the $y = x$ line is observed in this scatterplot. This is also true for the AA/3MA and 3MA/3DA comparison (Figures 12b and 12f). However, all of the AA/DHA, 3DA/DHA, and 3MA/DHA (Figures 12c, 12d, and 12e) scatterplots present a systematic bias which reveals among other things, the time shifting (1 month as a mean) often occurring between DHA and the other products. It is not surprising that the AA accordance is better with 3DA than with 3MA, as the three-dimensional model integrates more physics than the linear model. However, the better agreement that is found between 3DA and other than between 3DA and DHA reveals that besides data uncertainties, the 1986–1988 mean used for AA

and 3DA still contains an important interannual part with reference to the climatological mean taken for DHA over one century. This will be investigated further.

4. INTERANNUAL VARIABILITY

Basinwide Description

We can now consider, from November 1986 to November 1988, the monthly time evolution of the sea level and DH anomalies as given by the data and the models. Figures 13–19 present the basinwide situation for different months over all the years.

November 1986 (Figure 13) presents the same patterns as the climatological DH. It is interesting to note in the NECC high (positive anomaly at 3°–7°N) the presence of two distinct cells: one between 35° and 50°W and the other one east of 32°W, which are only shown by 3DA and are shown even more clearly by AA. This division in two different cells during the NECC decrease had also been observed in the

Fig. 22. Same as Figure 20 except for the South Equatorial Current region (2°N–2°S). Same gray scale as in Figure 1.

past [*Boisvert*, 1967; *Richardson and McKee*, 1984; *Arnault*, 1987] using ship drift data. However, several authors remained skeptical and argued that this division was perhaps only due to irregular data sampling. As this reason cannot be involved here, either for satellite data or for model results, the NECC disappears during the fall in two different cells.

In March 1987 (Figure 14), when the winds over the equatorial region are low, the AA extrema are stronger than the model ones by at least 3–6 cm. The location of the negative extremum around 3°N differs for 3DA (offshore the African coast) compared to the other quantities where it is offshore Brazil. It has been shown [*Richardson and McKee*, 1984; *Arnault*, 1987] that the NECC evolution, and thus the northern high associated with its geostrophic component, depends on the longitude. Its decrease starts from the west during the winter-fall season, and its strengthening first affects the eastern part of the basin. Thus the difference of the maximum location between 3DA and the other quantities could be only due to a time shifting. Moreover, 1 month later (not shown here), 3DA show a western negative anomaly.

In July 1987 the equatorial upwelling has begun (Figure 15). The negative signal of the equatorial upwelling reaches its maximal extension for all except for AA which present a more intense upwelling signal 1 month earlier. Compared to DHA where they are below −9 cm, the 1987 upwelling negative values are only about −6 cm for the models and −3 cm for AA. The other negative values (−6/9 cm), which appear along 10°N in AA are hardly outlined by the models, and shifted southward for 3MA.

The October 1987 situation (Figure 16) looks like those of November 1986 with a rather good agreement between AA and 3DA.

In March 1988 (Figure 17), differences compared to 1987 appear. First, the negative extremal values along 3°–5°N presented by 3DA are now along the Brazilian coast, in good agreement with AA, DHA, and 3MA. Second, north of 5°S, the Gulf of Guinea is affected by a positive anomaly which is stronger at least by a factor of 2 than in 1987. It can be interesting to compare this 1988 signal to those which occurred in 1984, 1 year after the 1982–1983 "El Niño"
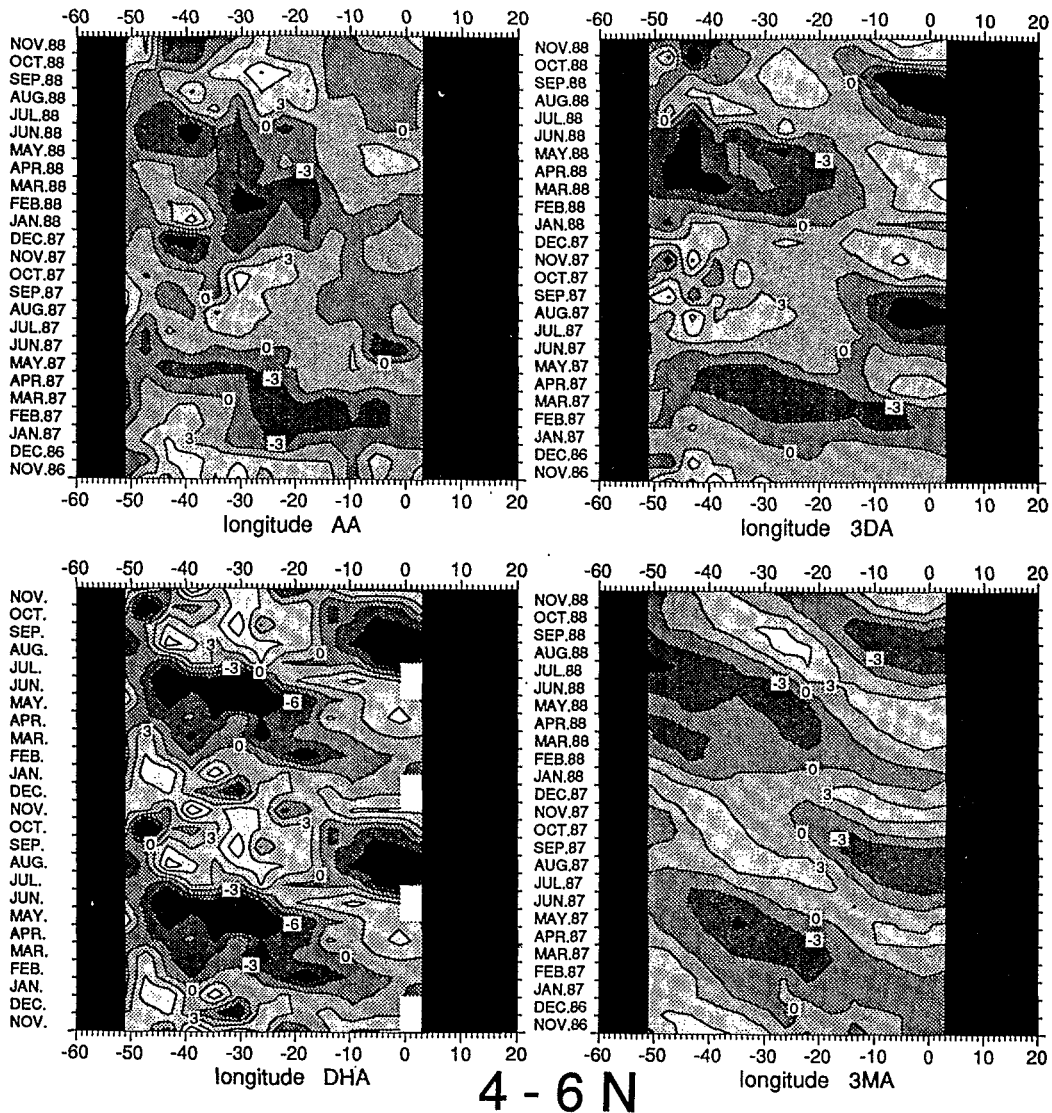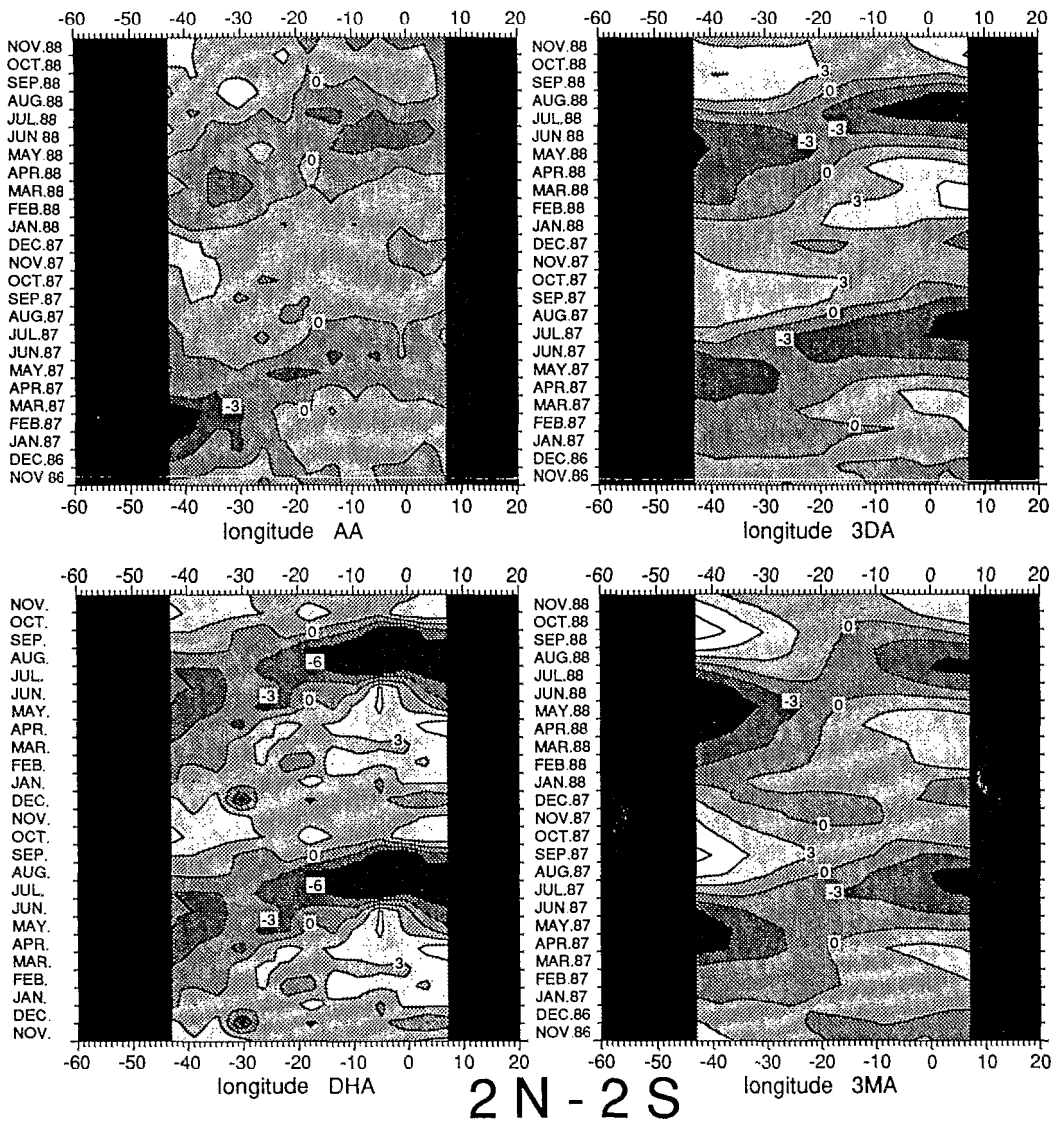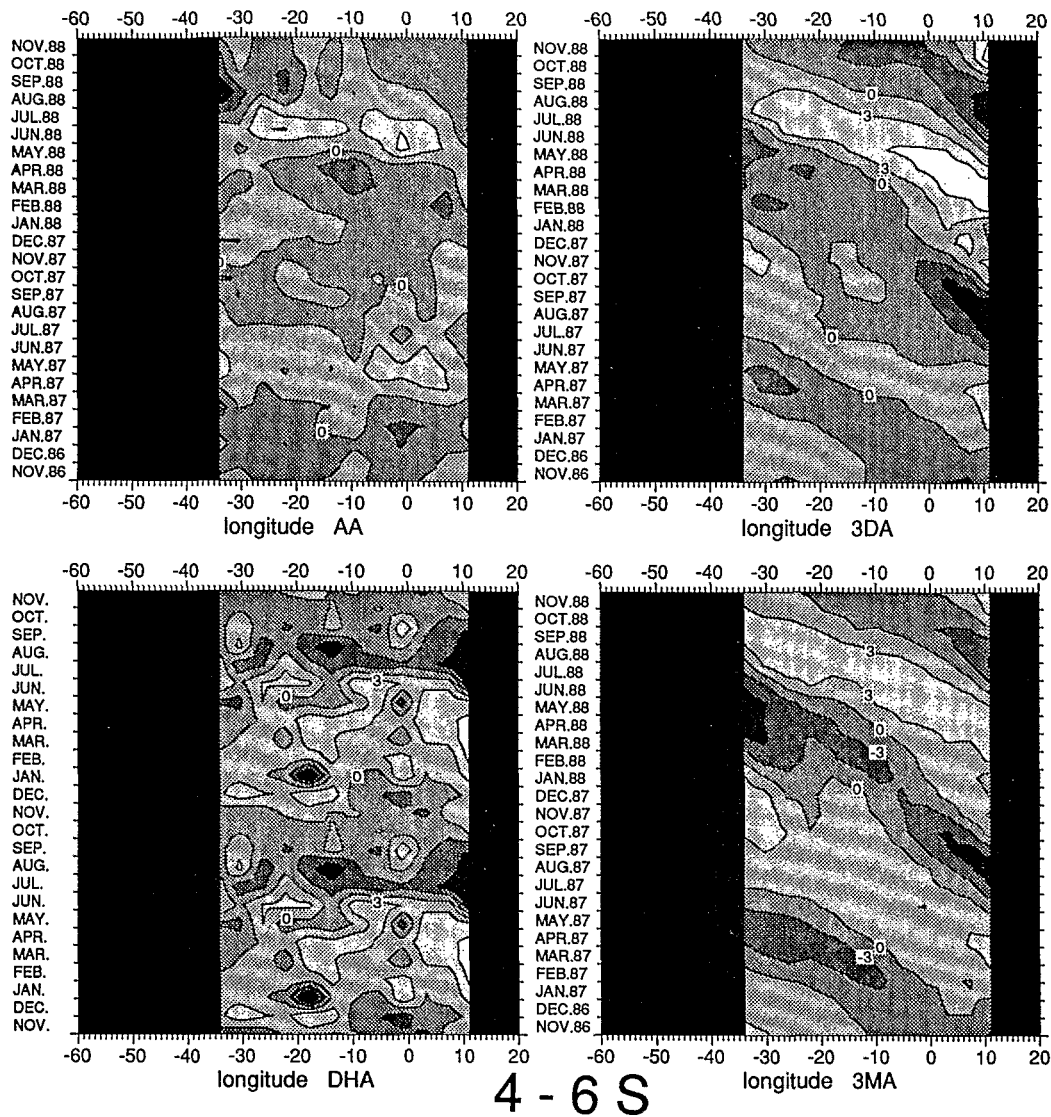
Fig. 23. Same as Figure 20 except for the South Equatorial Countercurrent region (4°–6°S). Same gray scale as in Figure 1.

phenomenon in the Pacific Ocean. During spring 1984 the Atlantic shows an unusual flat topography with the presence of warm water along the equator [*Hisard and Hénin*, 1987]. In terms of anomaly, equatorial warm water during the spring season mean a strong positive anomaly of the sea level with reference to its mean value. In 1986–1987 there was another El Niño in the Pacific. Therefore positive values in the Gulf of Guinea stronger in March 1988 than in 1987 are not surprising and could be linked to an El Niño event in the Pacific as in 1984. Even if the AA signal is less intense, this interannual warm event is also present.

In July 1988 (Figure 18) the negative values relative to the equatorial upwelling seem to be stronger than in 1987 for AA and the models, even if the satellite data results are still weak. The situation is therefore different from those in 1984 where the warm event remained during the boreal summer. It is also interesting to see for AA, DHA, and 3DA, the separation of the negative patch between 5° and 10°N in two different cells east and west of 40°W. Also clearly shown, but th time by AA, 3DA, and 3MA, are the two positive cells

located along 5°N and 5°S, which could be related to Rossby wave propagation. They were not so evident in 1987, except for AA.

Finally, in October 1988 (Figure 19) the positive anomaly at 3°N seems to be weaker than in 1987 for AA, 3DA, and 3MA, so that the NECC could have weakened earlier in 1987 than in 1988. This has been confirmed during a cruise in late September–October 1988 across the Atlantic. The hydrological data sampled during this campaign do not reveal any NECC high at 3°–5°N, as should be for this period [*Arnault et al.*, 1992]. It is also interesting to note the good agreement between AA and 3DA, showing the same eddy structures along 5°N, alternatively cyclonic and anticyclonic. However, in the Gulf of Guinea the AA signal is weaker again than the models' signal.

This first approach of the interannual variability in the tropics confirms our belief that the tropical Atlantic has been affected by relatively strong interannual events in 1986–1988 as was the case in 1983–1984. Time plots will confirm this hypothesis.
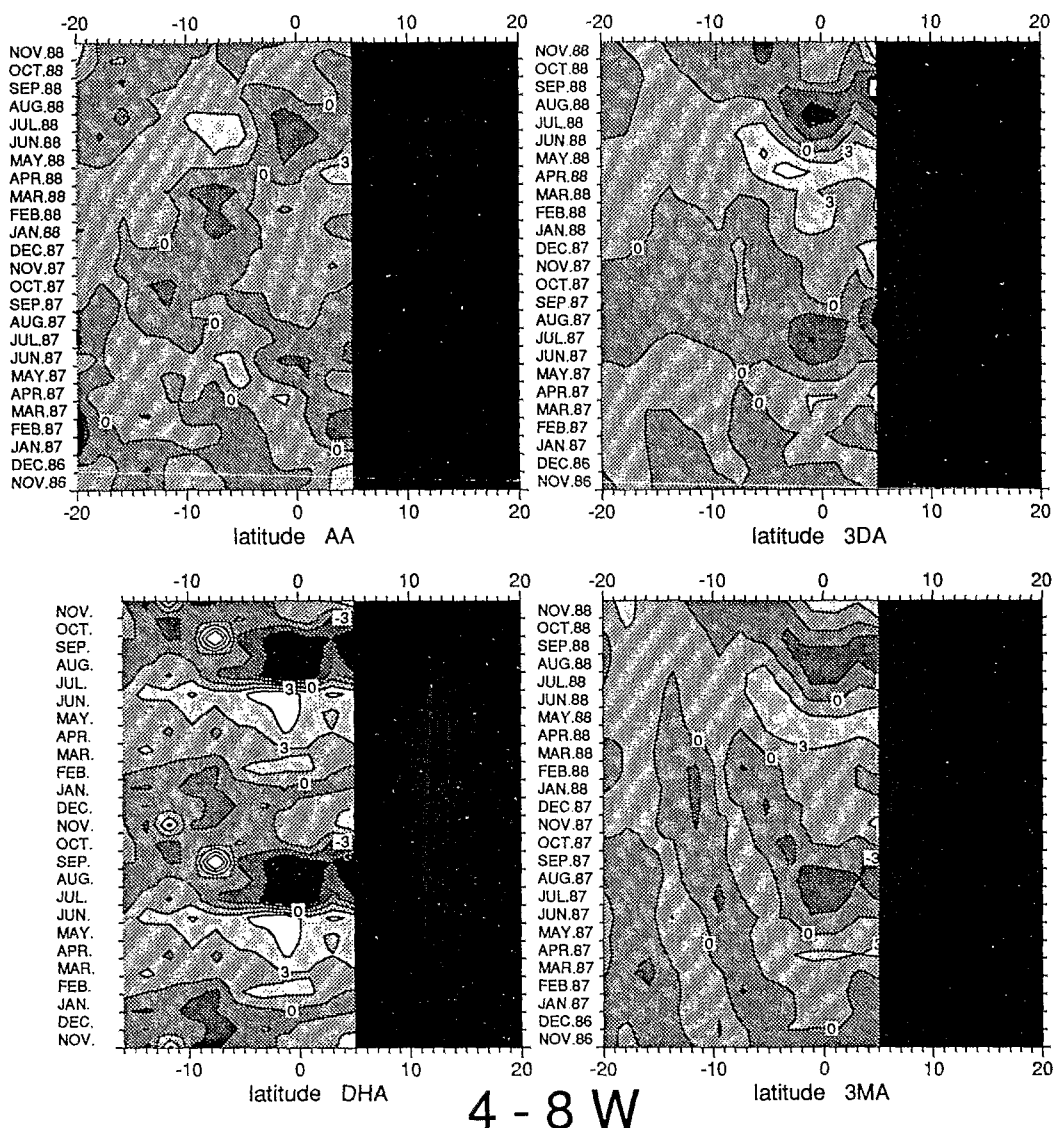
Fig. 24. Seasonal evolution along 4°–8°W for the 0/500 dbar in situ dynamic height anomalies (DHA in dynamic centimeters), and from November 1986 to November 1988 for the altimetric anomalies (AA in centimeters), the linear model 0/500 dbar dynamic height anomalies (3MA in dynamic centimeters) and for the three-dimensional model 5/500 dbar dynamic height anomalies (3DA in dynamic centimeters). Same gray scale as in Figure 1.

Longitudinal and Latitudinal Evolution for 1986–1988

Longitudinal evolution in the NEC region for 1986–1988. Between 14° and 16°N, in the NEC region (Figure 20) the signals are weak (3–6 cm), but the time shifting between AA, 3DA, 3MA, and DHA already evidenced by climatology (Figure 3) is even more pronounced. For example, models and AA present negative values between August and September, but otherwise DHA are mostly positive. It is also noteworthy that this signal is stronger in 1988 than in 1987, as revealed by AA, 3DA, or 3MA. Because of the interannual variability the rms for AA, 3DA, and 3MA computed between November 1986 and November 1988 (Table 2a) are slightly larger than the ones computed over the seasonal cycle. However, the rms differences AA/3DA, AA/3MA, and 3DA/3MA (Table 2b) are similar to those of Table 1b.

Longitudinal evolution in the NECC region for 1986–1988. The NECC region (Figure 21) comprises three different parts. West of 35°W, the situation is very complicated

with a lot of small-scale eddy structures. However, looking at AA and 3DA, it seems that the spring-summer negative values are stronger in 1988 than in 1987. Between 15° and 35°W, the signal is predominantly seasonal. The positive values here are higher in July–October 1988 than in 1987, but the maximum in 1988 occurs 1 month earlier, in September. AA and 3DA also depict a different intensification of the structures in 1987 and 1988: in 1987 the structures begin to change sign in March–April at 15°W. The positive extremum is reached around 30°W from July 1987 to October 1987. In 1988 the changing begins later, in April–May in the east, and lasts until September between 20° and 30°W. Finally, in the east the signal is semiannual, but it seems that the secondary negative extremum, which usually occurs in January–February, was hardly outlined in 1988 compared to 1987, as can be seen through AA, 3DA, or 3MA. The rms differences (Table 2b) for this period are very similar to the rms differences in Table 1b.
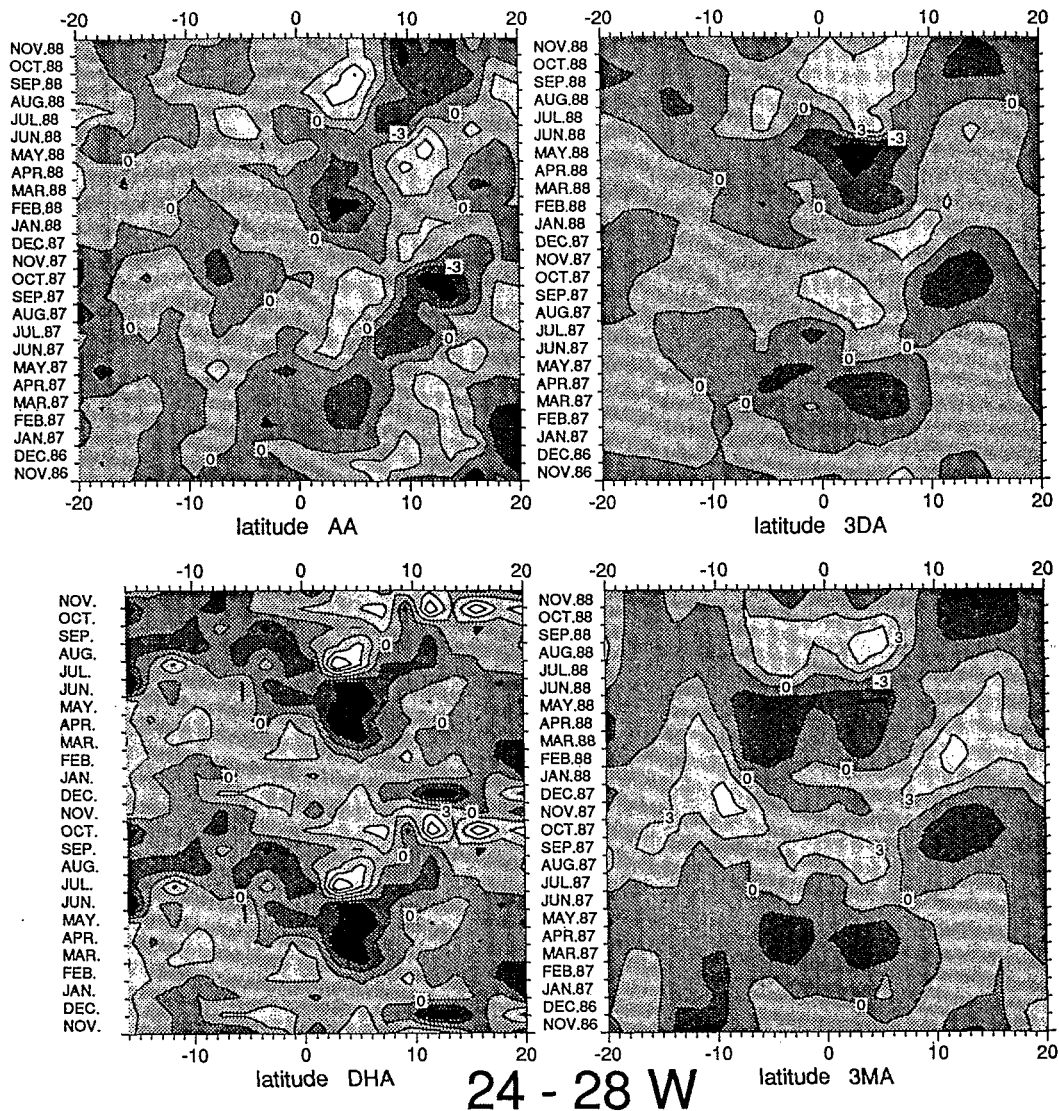
Fig. 25. Same as Figure 24 except for 24°–28°W. Same gray scale as in Figure 1.

Longitudinal evolution in SEC region for 1986–1988. West of 20°W, the AA and 3DA amplitudes are similar, but AA contrast with the models by presenting stronger negative anomalies in 1986–1987 than in 1988 (Figure 22). East of 20°W, 3DA and AA show a stronger negative upwelling signal in June–July 1988 than in 1987, but the AA signal is too weak and is time-shifted by about 1 month. Both present a secondary cold season in November–December 1987 and 1988, followed in January–March by a warm season as revealed by the positive anomaly which is stronger (3DA and 3MA) and longer (AA) in 1988 than in 1987.

Longitudinal evolution in SECC region for 1986–1988. In the southern hemisphere (Figure 23), even if the signal is more amorphous (−6, +6 cm), it still seems that the positive anomaly in spring-summer 1988 is stronger than in 1987. However, compared to the data, the models still emphasize the propagation phenomenon.

Latitudinal evolution in the Gulf of Guinea along 4°W and in the center of the basin along 28°W for 1986–1988. Along 4°W (Figure 24) the agreement between AA and 3DA is best compared with the other panels in Figure 24. North of 10°S,

AA and 3DA both show weaker anomalies in 1987 than in 1988 by more than 3 cm. This still persists at 28°W (Figure 25), especially in the northern hemisphere: even if the phase opposition presented by the signals between 0°–10°N on one hand and 10°–20°N on the other hand is clearly evidenced for both years, in 1987 the signals are weaker than in 1988.

The changes that affect the tropical Atlantic in 1988 compared to 1987 can also be depicted through local comparison. Once this is done, we will then be able to quantify the correlation between AA and 3DA.

Local Comparisons

Figures 26 and 27 present the comparison of the signals between November 1986 and November 1988. We just add the climatological year for DHA to compare with Figures 9 and 10.

In the western NECC (5°N–46°W) (Figure 26a), the better agreement is found between 3MA and AA as it was already true for the climatology (Figure 9a). The 3DA is clearly
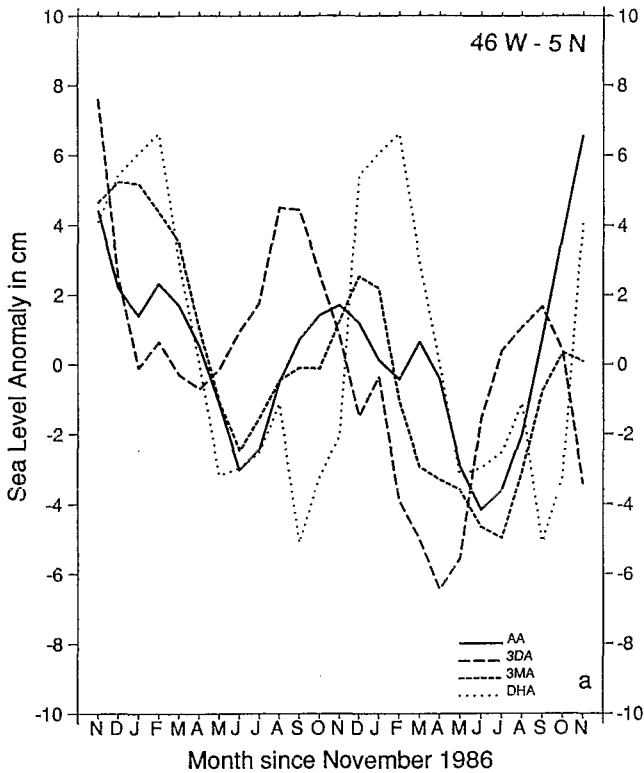
Fig. 26a. Comparison between November 1986 and November at 46°W–5°N. The in situ dynamic height anomalies' (DHA) in *dynamic centimeters*) seasonal cycle is only given as an indication. A running mean over 3 months is performed in order to eliminate small-scale noise.

time-shifted by 3 months at least. The amplitude of the 1986–1988 signals are mostly the same about 8–10 cm. AA, 3DA, and 3MA present a decrease of the mean between 1986 and 1988, as the positive extrema weaken (around 4 cm for AA in 1986, then 2 cm in 1987; more than 8 cm for 3DA in 1986, then 2 cm in 1988; 5 cm for 3MA in 1986, then 0 cm and the negative extrema strengthen (more than −3 cm for AA in 1987, then −4 cm in 1988; more than −1 cm for 3DA in 1986, then −6 cm; −3 cm for 3MA in 1987, then −5 cm). The correlation between AA and 3DA is only 0.5 due to the time shifting.

Eastward (Figure 26b), the agreement is better and reaches a 0.77 correlation coefficient between AA and 3DA. The extrema in summer 1988 (5–7 cm) seem to be stronger than in 1987 (less than 4 cm), but the minima in March–April are of the same order in 1988 as in 1987 (−4/5 cm). If AA, 3DA, and 3MA vary in phase in spring 1987, there is a 1-month lag during spring 1988 between AA and 3DA and 3DA and 3MA. This is due to the decrease toward the negative values which occurs faster (3 months) for AA than for models (5–6 months).

In the east (Figure 26c) the AA signal is flat compared with the others in July–August 1987. This explains why the correlation between AA and 3DA is only 0.53. However, for 3DA and AA, the extrema in June–August 1988 (−7 and −3 cm, respectively) are stronger than in 1987 (−6 and −1 cm). The values for the warm spring season are also stronger in 1988 (5 and 3 cm) than in 1987 (3 and 1 cm).

Farther south, in the SEC (Figure 27) at 1°N the correlation between AA and 3DA is better in the west (0.57, Figure 27a) than in the center (0.44 Figure 27b) or in the east (0.32,
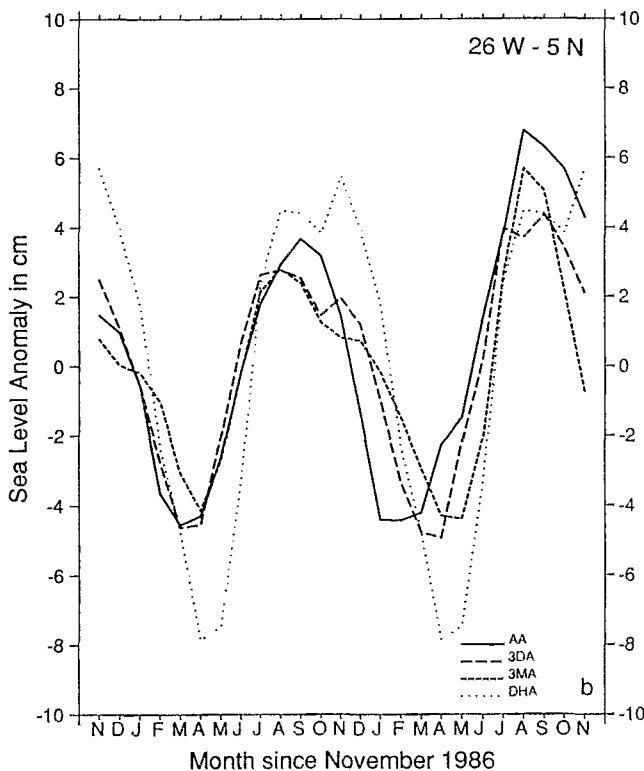

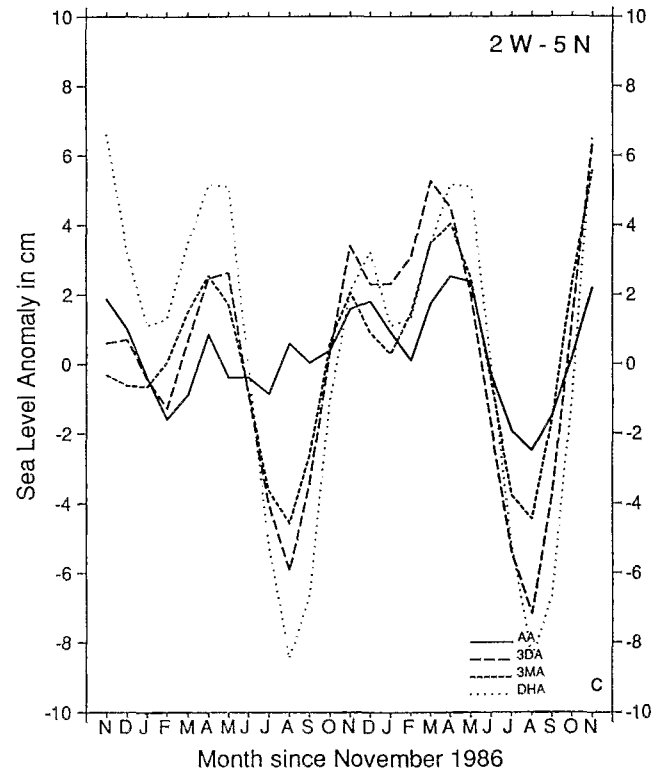Fig. 26b. Same as Figure 26a, except for 26°W–5°N.

Fig. 26c. Same as Figure 26a, except for 2°W–5°N.

Figure 27c). These bad correlations are once again explained by the lack of upwelling signal in AA in the summer of 1987.

Statistics

The good agreement which exists between AA and 3DA in the northwestern Atlantic Ocean is shown by the correlation coefficients given in Figure 28. A large part of this region present coefficients larger than 0.7. In the Gulf of Guinea, as already discussed, the correlation is low (less than 0.5). Regions where the signals are anticorrelated are few and located northward, southward, or near the American coast. The same conclusions can be derived from the comparison 3MA/AA. Finally, the extremely good temporal agreement between the two models is also depicted in Figure 28: a large part of the basin is covered by correlation up to 0.7.

The rms differences between the data are given in Figure 29. It is clear that the best agreement is always found between AA and 3DA with a mean value about 3.2 cm.

5. DISCUSSION AND CONCLUSIONS

We examined in this paper the comparison of four products (climatological DH, altimetry, linear, and three-dimensional model results) to obtain the most complete overview of the surface dynamic topography variability in the tropical Atlantic Ocean.

The seasonal cycle as shown by altimetry and models is in rather good agreement with the one presented by DH climatology. The seasonal variability is clearly stronger in the northern hemisphere. The Gulf of Guinea is affected by
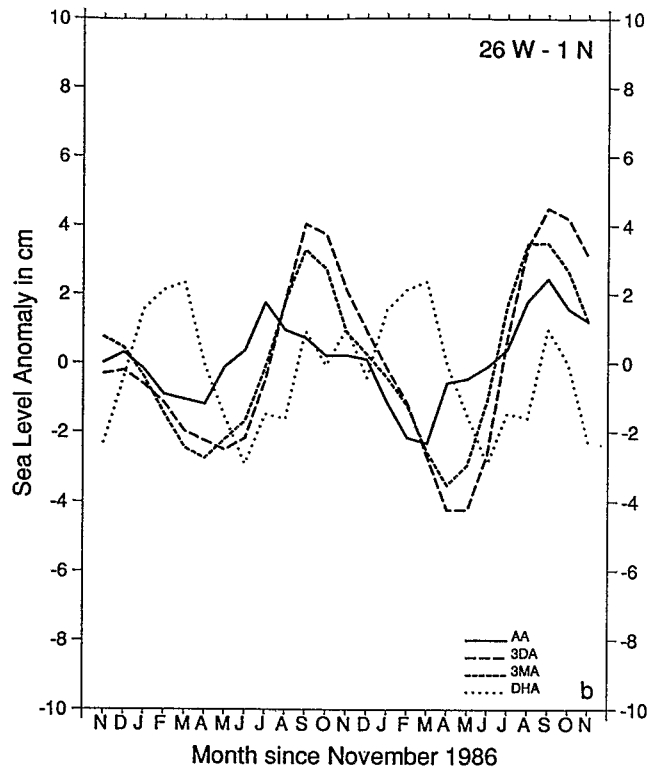
Fig. 27b. Same as Figure 26, except for 26°W–1°N.

a semimodal signal with two cold seasons, in December–January and in June–August. However, the altimetric variability is too small in this region compared with the other quantities. Westward propagation at 5°N, in the NECC, is
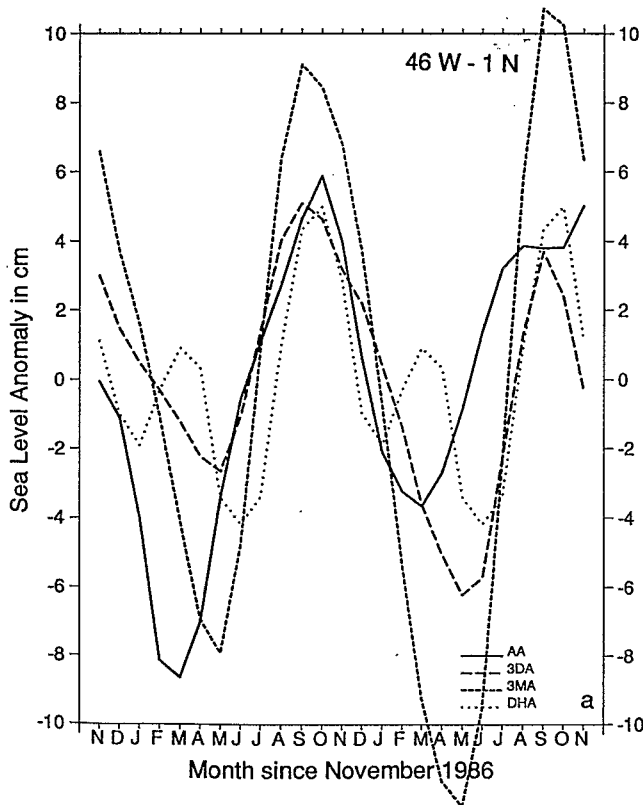
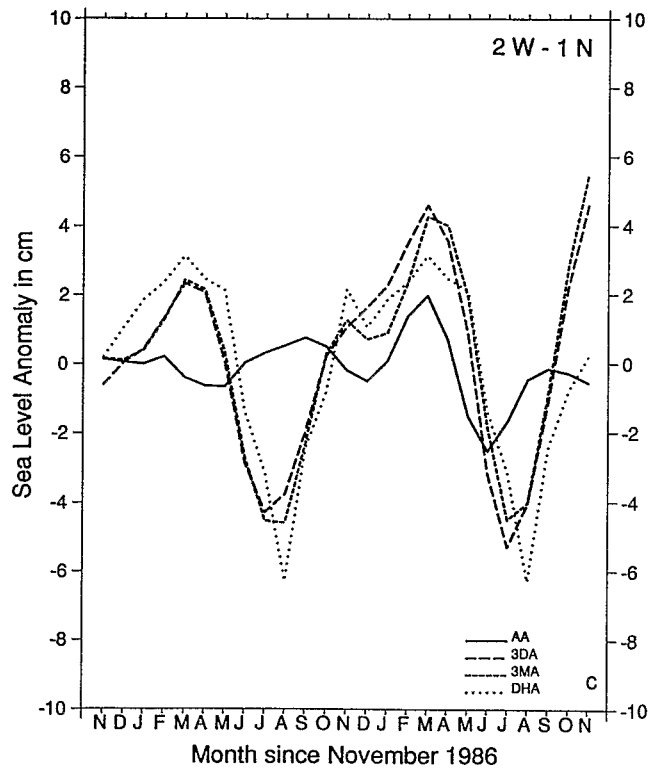Fig. 27a. Same as Figure 26, except for 46°W–1°N.

Fig. 27c. Same as Figure 26, except for 2°W–1°N.

above 0.7
0.5 - 0.7
0.0 - 0.5
below 0.0

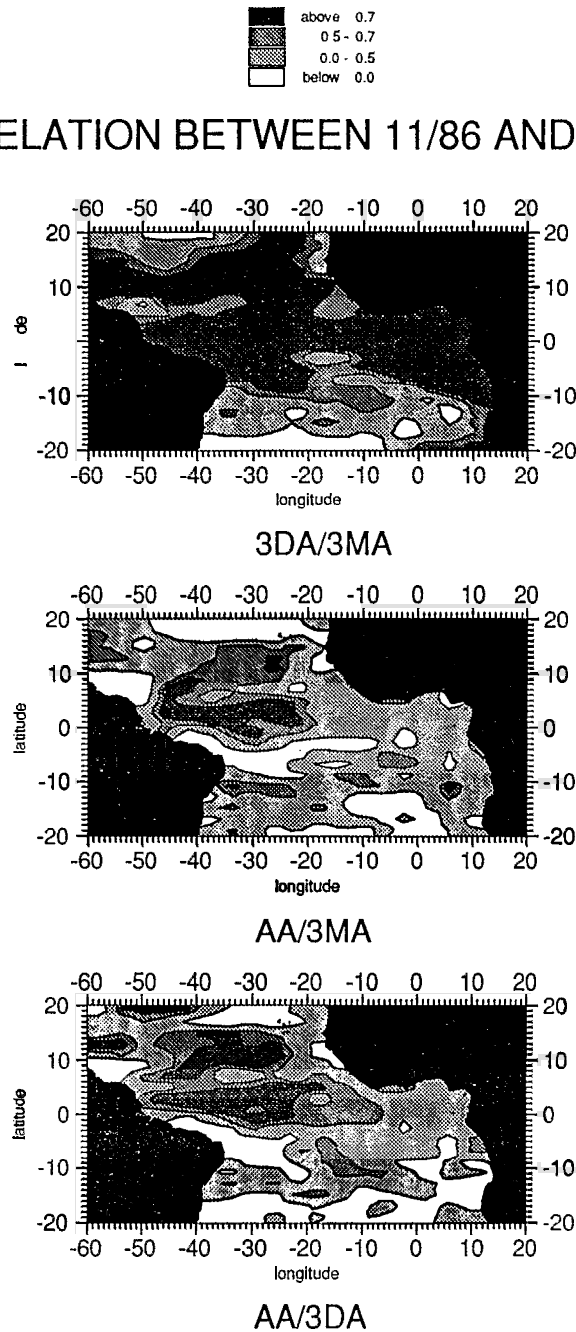## CORRELATION BETWEEN 11/86 AND 11/88

3DA/3MA

AA/3MA

AA/3DA

Fig. 28. Correlation coefficients computed in the tropical Atlantic Ocean for the November 1986 to November 1988 period between the altimetric anomalies and the three-dimensional model 5/500 dbar dynamic height anomalies (AA/3DA), the altimetric anomalies and the linear model 0/500 dbar dynamic height anomalies (3MA/AA), and the three-dimensional model 5/500 dbar dynamic height anomalies and the linear model 0/500 dbar dynamic height anomalies (3DA/3MA).

clearly shown by all the data and models, but at 5°S, such a propagation is only present in the models. The annual variability is maximal in the western basin, along 2°–3°N and 10°N. These maxima are separated by a minimum much more evident for altimetry and models than for the climatological DH. We do assume that most of the differences encountered between altimetry/models on one hand and DH climatology on the other hand are due to the mean being computed over 2 years for altimetry and models and over a century for the climatology. Therefore the altimetric/model averages involve interannual information that has been con-

siderably filtered out in the climatological mean. This explains that the best rms differences between models and data are found between three-dimensional model and altimetry with a mean value of 2.6 cm.

The study of the 1986–1988 cycles has confirmed the good agreement between altimetry and models (Figure 30). It also points out several features. First, the NECC region can be divided in two parts during the fall decrease: two different cells appear east and west of 30°–35°W. It seems to be a constant feature as it is observed in October 1986, November 1987, and November 1988 from altimetry and models.
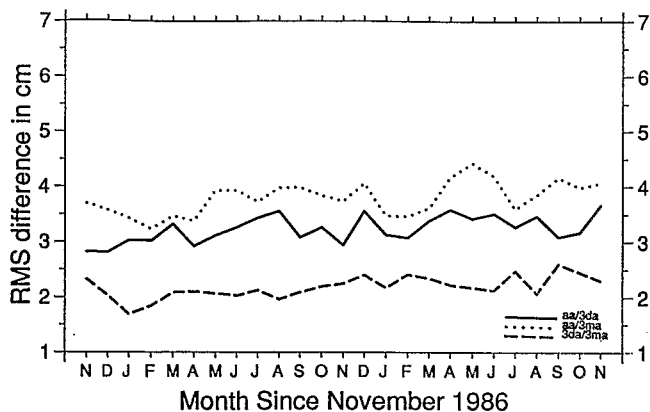
1986-1988

Fig. 29. Mean rms differences (in centimeters) from November 1986 to November 1988 between altimetry and three-dimensional model anomalies (solid line), altimetry and linear model anomalies (spaced dotted line), and three-dimensional model and linear model anomalies (long dashed line).

AA/3MA 86-88

Fig. 30b. Same as Figure 30a, except for altimetric anomalies and linear model results (AA/3MA).

Although it had been observed in the past, many authors were suspicious about this division and argued that it could be due to an artifact of in situ data sampling, which is obviously not the case for altimetry and models. Second, also pointed out by this study, is the presence of interannual events in the tropical Atlantic Ocean. It has been widely assumed in the past that contrary to the Indian or the Pacific oceans, the annual cycle is dominant in the tropical Atlantic. However, in particular, since the 1982–1984 Programme Français Océan Climat en Atlantique Equatorial (FOCAL)/ Seasonal Response of the Equatorial Atlantic (SEQUAL) programs, the presence of strong interannual events has

been shown especially in the Gulf of Guinea, 1 year after the El Niño Pacific phenomenon. The following explanation has been enounced: when an El Niño occurs in the Pacific Ocean, warm waters piled up on the eastern side of the Pacific basin result in a Walker cell displacement. As a consequence, the trade winds over the west Atlantic intensify as does the oceanic pressure gradient. Several months later, when the Walker cell returns to its usual location, the Atlantic winds relax. The Atlantic pressure gradient is no

AA/3DA 86-88

Fig. 30a. Scatterplot for the November 1986 to November 1988 period between altimetric anomalies and three-dimensional results (AA/3DA).

3DA/3MA 86-88
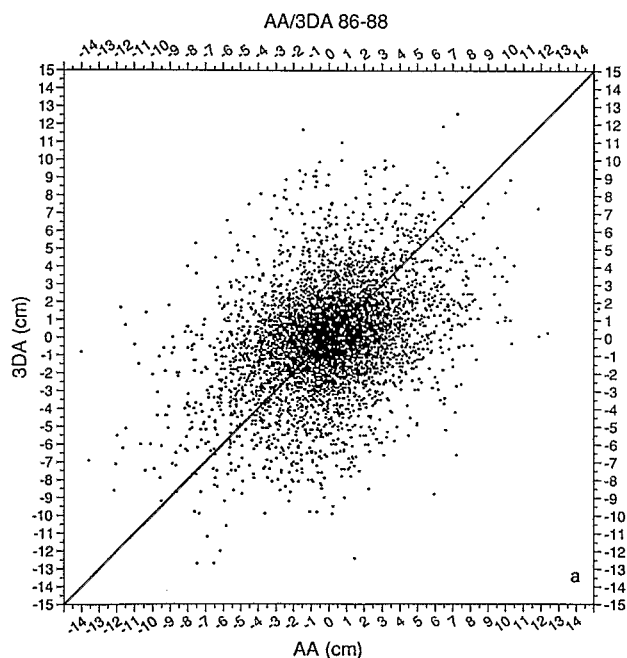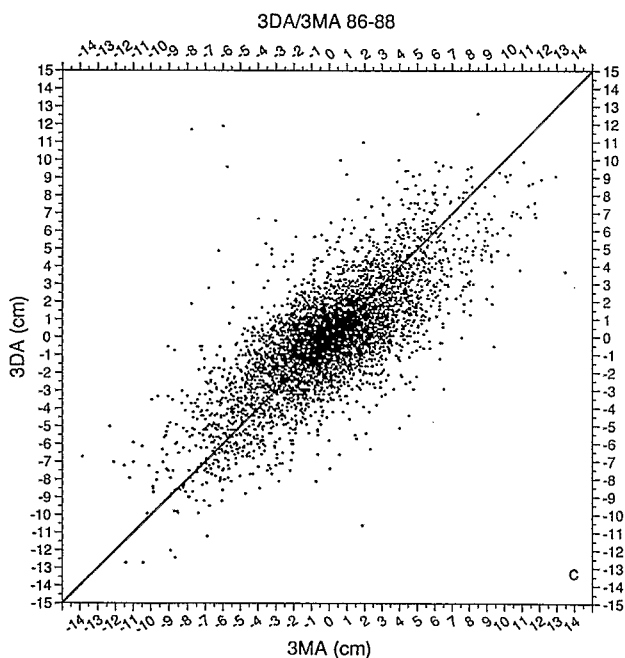

Fig. 30c. Same as Figure 30a, except for three-dimensional model and linear model results (3DA/3MA).
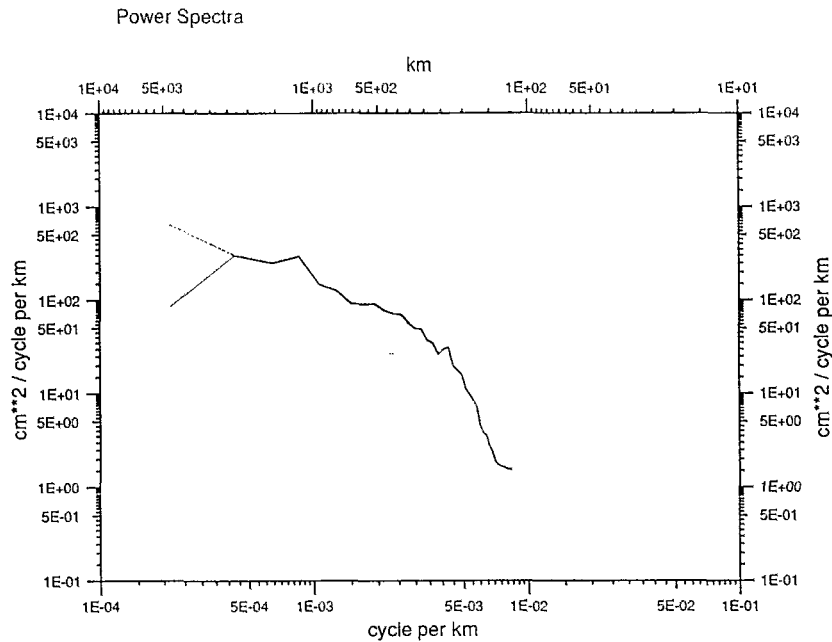
Power Spectra

Fig. 31. Power spectra along a characteristic descending track in the Gulf of Guinea. Using a long track (40°S), GDR or GEM-T2 orbits, and a second-degree polynomial adjustment (solid line); using a long track (40°S), GDR or GEM-T2 orbits, and a one-degree polynomial adjustment (dashed line); and using a short track (20°S), GDR or GEM-T2 orbits, and a 1° polynomial adjustment (dotted line).

longer in equilibrium with the wind stress forcing, and the warm waters accumulated in the west flow back into the Gulf of Guinea. In 1982–1983, a strong El Niño occurred in the Pacific, and in spring 1984 the FOCAL/SEQUAL data showed abnormal warm waters in the east Atlantic with a flat thermocline and no pressure gradient all along the equator [*Philander*, 1986; *Lamb et al.*, 1986; *Weisberg and Colin*, 1986; *Hisard et al.*, 1986; *Katz et al.*, 1986]. In 1986–1987, another El Niño was detected in the Pacific, also not as intense as the 1982–1983 one, and the sea surface temperature maps obtained by *Servain and Lukas* [1990] reveal abnormally warm waters in the Gulf of Guinea during spring 1988. During spring 1988, altimetry and models also show waters in the Gulf of Guinea that are warmer than in 1987. However, the altimetric signal was weaker than the model ones.

We tried to discover why the altimetric signal was so weak in the Gulf of Guinea. As described in section 2, altimetric data have to be corrected and filtered out first before producing the "real" oceanic sea level signal. *Ménard* [1988] has already approached the same problem, but he used different techniques and corrections. One of the corrections which could be particularly important in the tropics is the water vapor correction. As *Ménard* [1988], we used the FNOC water vapor correction. Recent investigations have revealed that differences between several water vapor products could be important. In the equatorial Pacific, *Zimbelman and Busalacchi* [1990] found for the FNOC and SMMR corrections a mean rms difference ranging from 2 cm to more than 8 cm in December 1983. *Emery et al.* [1990] have computed altimetric corrections from FNOC, Tiros-N operational vertical sounder Seasat scanning multichannel microwave radiometer (SMMR), and special sensor microwave imager water vapor. They found that the FNOC-derived

corrections are generally much too low in the tropics. Along a Geosat track in the Atlantic, they found a difference between FNOC and SMMR corrections of about 10 cm around 7°N. Therefore we recomputed for three tracks in the Gulf of Guinea the sea level anomalies, using either FNOC or SMMR water vapor corrections. These along-track sea level anomalies differ only slightly, and the resulting mean rms differences vary around 1 cm. This low value is due to the altimetric data processing which only implies "anomalies." *Zimbelman and Busalacchi* [1990] found that the mean rms differences between different water vapor products are divided by a factor of 2 if the respective mean field is first subtracted. Moreover, along-track power spectra reveal that most of the difference found in our analysis referred to wavelengths over 2000 km (Figure 31).

Another investigation leads us to consider the effect of the orbit error. We used the Geosat operational orbits which are available from *Cheney et al.* [1987]. *Born et al.* [1988] have estimated that the radial component of these orbits is accurate to about 3 m rms. Fortunately, the largest component of the error occurs at a wavelength equal to the orbital circumference. Thus a large percentage of the error can be removed on a regional basis using simple adjustment techniques in which the error is modeled as a low-order polynomial [*Cheney et al.*, 1989]. But this filter can also eliminate signals of the large-scale ocean circulation. Therefore significant benefit could be derived from using precise orbits. We recomputed the altimetric signal along the same three tracks we already used in the Gulf of Guinea for the water vapor study. However, we now use longer tracks (up to 40°S instead of 20°S) and the new orbit computation based upon GEM-T2 gravity field. *Haines et al.* [1990] have shown that the use of GEM-T1 gravity solution reduced the estimated radial orbit error from the level of 3 m rms to about a 85-cm

level. They suggested that with GEM-T2 the radial orbit accuracies would be about 35 cm rms. The results of our investigation are that using the same track length (up to 40°S) and the same polynomial adjustment but with two different orbits, the rms difference is about 0.50 cm for a 1° polynomial adjustment, and it is 2 cm for a second-order polynomial adjustment. Using the same track length (up to 40°S) and the same orbit but different polynomial adjustment (first- or second-order polynomial adjustment), the mean rms difference is between 2 and 3 cm, but power spectra reveal that only the wavelengths over 2000 km are affected by these changes. However, the use of a shorter track (up to 20°S) indicates a lack of energy even for short wavelengths (200 km) (Figure 31). Considering the particular shape of the African coast, due to the presence of the meridional Gabon-Angola coasts to the east and the zonal Guinea-Togo coasts to the north, almost all Geosat ascending tracks are considerably short with no possibility of extension. Thus as mentioned earlier, the altimetric signal is then reduced, and this certainly explains the differences encountered between altimetry and three-dimensional model in the Gulf of Guinea.

Therefore the global patterns of the seasonal cycle of the tropical Atlantic surface topography are identically represented by the altimetric observations and the model simulations and are in agreement with former dynamic height climatology. The better correlation is found between altimetry and a three-dimensional model for both the seasonal signal and the interannual variability. For the future altimetric mission, such as the next TOPEX/Poseidon mission, microwave radiometer will be on board, and high accuracy ground tracking will be performed. The radial orbit error should then be about 10 cm. Therefore using longer descending track, better orbit correction, and lighter adjustment, probably the quality of the altimetric signal in the Gulf of Guinea will be as it is already elsewhere in the tropical Atlantic Ocean. The association of these future altimetric data with a three-dimensional model will provide the best approach to the large-scale variability in the tropical ocean.

REFERENCES

Arnault, S., Tropical Atlantic geostrophic currents and ship drifts, *J. Geophys. Res.*, 92(C5), 5076–5088, 1987.

Arnault, S., Y. Ménard, and J. Merle, Observing the tropical Atlantic Ocean in 1986–1987 from altimetry, *J. Geophys. Res.*, 95(C10), 17,921–17,945, 1990.

Arnault, S., L. Gourdeau, and Y. Ménard, Comparison of the altimetric signal with in-situ measurements in the tropical Atlantic Ocean, *Deep Sea Res.*, 39(3/4), 481–499, 1992.

Boisvert, L., Major currents in the north and south Atlantic Ocean between 64°N and 60°S, *Tech. Rep.*, 193, U.S. Naval Oceanogr. Off., Washington, D. C., 1967.

Born, G. H., F. G. Lemoine, and M. J. Crawford, Geosat ERM orbit determination, *Adv. Astron. Sci.*, 65, 425–446, 1988.

Busalacchi, A., and J. Picaut, Seasonal variability from a model of the tropical Atlantic Ocean, *J. Phys. Oceanogr.*, 13, 1564–1588, 1983.

Cane, M. A., The response of an equatorial ocean to simple wind stress patterns, II, Numerical results, *J. Mar. Res.*, 37(2), 253–299, 1979.

Cane, M. A., and T. Sarachik, The response of a linear baroclinic equatorial ocean to periodic forcing, *J. Mar. Res.*, 39, 651–693, 1981.

Carton, J. A., Estimates of sea level in the tropical Atlantic Ocean using Geosat altimetry, *J. Geophys. Res.*, 94(C6), 8029–8039, 1989.

Cartwright, D. E., and R. J. Taylor, New computations of the tide generating potential, *Geophys. J. R. Soc. London*, 23, 45–74, 1971.

Chartier, M., Un modèle numérique tridimensionnel aux équations primitives de circulation générale de l'océan, thèse, Univ. Paris 6, Paris, 1985.

Cheney, R. E., J. G. Marsh, and B. D. Beckley, Global mesoscale variability from collinear tracks of Seasat altimeter data, *J. Geophys. Res.*, 88(C7), 4343–4354, 1983.

Cheney, R. E., B. C. Douglas, R. W. Agreen, L. L. Miller, and D. L. Porter, Geosat altimeter Geophysical Data Record (GDR) user handbook, 23 pp., Natl. Ocean Surv., Natl. Ocean. Atmos. Admin., Washington, D. C., 1987.

Cheney, R. E., B. C. Douglas, and L. L. Miller, Evaluation of Geosat altimeter data with application to tropical Pacific sea level variations, *J. Geophys. Res.*, 94(C4), 4737–4747, 1989.

Daniault, N., and Y. Ménard, A comparison of eddy kinetic energy distribution in the southern ocean from Seasat altimeter and FGGE free drifting buoys, *J. Geophys. Res.*, 90(C6), 11,877–11,890, 1985.

De Mey, P., and A. R. Robinson, Simulation and assimilation of satellite altimeter data at the oceanic mesoscale, *J. Phys. Oceanogr.*, 17, 2280–2293, 1987.

Douglas, B. C., R. E. Cheney, and R. W. Agreen, Eddy energy of the northwest Atlantic and Gulf of Mexico determined from GEOS 3 altimetry, *J. Geophys. Res.*, 88(C14), 9595–9603, 1983.

du Penhoat, Y., and Y. Gouriou, Hindcasts of equatorial sea surface dynamic height in the Atlantic in 1982–1984, *J. Geophys. Res.*, 92(C4), 3729–3740, 1987.

du Penhoat, Y., and A. M. Tréguier, The seasonal linear response of the tropical Atlantic Ocean, *J. Phys. Oceanogr.*, 15, 316–329, 1985.

Eckart, C., Properties of water, part II, The equation of water and sea water at low temperatures and pressures, *Am. J. Sci.*, 256, 225–240, 1958.

Emery, W. J., G. H. Born, D. G. Baldwin, and C. L. Norris, Satellite-derived water vapor corrections for Geosat altimetry, *J. Geophys. Res.*, 95(C3), 2953–2964, 1990.

Esbensen, S. K., and Y. Kushnir, The heat budget of the global ocean: An atlas based on estimates from marine surface observations, *Rep. 29*, 27 pp., Clim. Res. Inst., Oreg. State Univ., Corvallis, 1981.

Fu, L., On the wave number spectrum of oceanic mesoscale variability observed by Seasat altimeter, *J. Geophys. Res.*, 88(C7), 4331–4342, 1983.

Haines, B. J., G. H. Born, G. W. Rosborough, J. G. Marsh, and R. G. Williamson, Precise orbit computation for the Geosat exact repeat mission, *J. Geophys. Res.*, 95(C3), 2871–2885, 1990.

Hellerman, S., and M. Rosenstein, Normal monthly wind stress over the world ocean with error estimates, *J. Phys. Oceanogr.*, 13, 1093–1104, 1983.

Hisard, P., and C. Hénin, Response of the equatorial Atlantic Ocean to the 1983–1984 wind from the Programme Français Océan et Climat dans l'Atlantique Equatorial cruise data set, *J. Geophys. Res.*, 92(C4), 3759–3768, 1987.

Hisard, P., C. Hénin, R. Houghton, B. Piton, and P. Rual, Oceanic conditions in the tropical Atlantic during 1983 and 1984, *Nature*, 322(6076), 243–245, 1986.

Katz, E. J., Dynamic topography of the sea surface in the equatorial Atlantic, *J. Mar. Res.*, 39(1), 53–63, 1981.

Katz, E. J., Seasonal response of the sea surface to the wind in the equatorial Atlantic, *J. Geophys. Res.*, 92(C2), 1885–1893, 1987.

Katz, E. J., P. Hisard, J. M. Verstraete, and S. L. Garzoli, Annual change of sea surface slope along the equator of the Atlantic Ocean in 1983 and 1984, *Nature*, *322*(6076), 245–247, 1986.

Lamb, P. J., R. A. Peppler, and S. Hastenrath, Interannual variability in the tropical Atlantic, *Nature*, *322*(6076), 238–240, 1986.

Large, W. G., and S. Pond, Open ocean momentum flux measurements in moderate strong winds, *J. Phys. Oceanogr.*, *11*, 324–336, 1981.

Lass, H. U., V. Bubnov, J. M. Huthnance, E. J. Katz, J. Meincke, A. de Mesquita, F. Ostapoff, and B. Voituriez, Seasonal changes of the zonal pressure gradient in the equatorial Atlantic during the FGGE year, *Oceanol. Acta*, *6*, 3–11, 1987.

Leetmaa, A., and M. Ji, Operational hindcasting of the tropical Pacific, *Dyn. Atmos. Oceans*, *13*(3–4), 1989.

Levitus, S., Climatological atlas of the world ocean, *Prof. Pap. 13*, 173 pp., Natl. Oceanic and Atmos. Admin., Washington, D. C., 1982.

Malarde, J. P., P. De Mey, C. Perigaud, and J. F. Minster, Observation of long equatorial waves in the Pacific Ocean by Seasat altimetry, *J. Phys. Oceanogr.*, *17*, 2273–2279, 1987.

Ménard, Y., Observation of eddy fields in the northwest Atlantic and the northwest Pacific by Seasat altimeter data, *J. Geophys. Res.*, *88*(C3), 1853–1866, 1983.

Ménard, Y., Observing the seasonal variability in the tropical Atlantic from altimetry, *J. Geophys. Res.*, *93*(C11), 13,967–13,978, 1988.

Merle, J., and S. Arnault, Seasonal variability of the surface dynamic topography in the tropical Atlantic Ocean, *J. Mar. Res.*, *43*, 267–288, 1985.

Miller, L., R. E. Cheney, and D. Milbert, Sea level time series in the equatorial Pacific from satellite altimetry, *Geophys. Res. Lett.*, *13*, 475–478, 1986.

Millero, J., and A. Poisson, The practical salinity scale 1978 and the international equation of state of the sea water 1980, *Rep. 10*, U.N. Educ. and Sci. Cult. Org., New York, 1981.

Morlière, A., P. Delecluse, P. Andrich, and B. Camusat, Evaluation des champs thermiques simulés par un modèle de circulation générale de l'Atlantique tropical, *Oceanol. Acta*, *12*(1), 9–22, 1989.

Musman, S., Sea slope changes associated with westward propagating equatorial temperature fluctuations, *J. Geophys. Res.*, *91*(C9), 10,753–10,757, 1986.

Périgaud, C., J. F. Minster, and G. Reverdin, Zonal slope variability of the tropical Indian Ocean studied from Seasat altimetry, *Mar. Geod.*, *10*, 53–67, 1986.

Philander, S. G. H., Unusual conditions in the tropical Atlantic Ocean in 1984, *Nature*, *322*(6076), 236–238, 1986.

Philander, S. G. H., and R. C. Pacanowski, Response of equatorial oceans to periodic forcing, *J. Geophys. Res.*, *86*(C3), 1903–1916, 1981.

Philander, S. G. H., and R. C. Pacanowski, A model of the seasonal cycle in the tropical Atlantic Ocean, *J. Geophys. Res.*, *91*(C12), 14,192–14,206, 1986.

Reverdin, G., and Y. du Penhoat, Modeled surface dynamic height in 1964–1984: An effort to assess how well the low frequencies in the equatorial Atlantic were sampled in 1982–1984, *J. Geophys. Res.*, *92*(C2), 1899–1913, 1987.

Reverdin, G., P. Delecluse, C. Levi, P. Andrich, A. Morlière, and J. M. Verstraete, The near surface tropical Atlantic in 1982–1984, results from a numerical simulation and a data analysis, *Prog. Oceanogr.*, *27*, 273–340, 1991.

Richardson, P., and T. McKee, Average seasonal variation of the Atlantic equatorial currents from historical ship drifts, *J. Phys. Oceanogr.*, *14*, 1226–1238, 1984.

Richardson, P. L., and G. Reverdin, Seasonal cycle of velocity in the Atlantic North Equatorial Countercurrent as measured by surface drifters, current meters and ship drifts, *J. Geophys. Res.*, *92*(C4), 3691–3708, 1987.

Saastamoinen, J., Atmospheric correction for troposphere and stratosphere in radio ranging of satellites, in *The Use of Artificial Satellites for Geodesy, Geophys. Monogr. Ser.*, vol. 15, edited by S. W. Henriksen, A. Mancini, and B. H. Chovitz, pp. 247–252, AGU, Washington, D. C., 1972.

Schwiderski, E. W., On charting global tides, *Rev. Geophys.*, *18*(1), 243–268, 1980.

Servain, J., and S. Lukas, Climatic atlas of the tropical Atlantic wind stress and sea surface temperature: 1985–1989, in *Climatic Atlas of the Tropical Atlantic Wind Stress and Sea Surface Temperature: 1985–1989*, Centre ORSTOM de Brest, IFREMER, Plouzané, France, 1990.

Servain, J., M. Seva, S. Lukas, and G. Rougier, Climatic atlas of the tropical Atlantic wind stress and sea surface temperature: 1980–1984, *Ocean Air Interaction*, *1*, 109–182, 1987.

Tapley, B. D., J. B. Lundberg, and G. H. Born, The Seasat altimeter wet tropospheric range correction, *J. Geophys. Res.*, *87*(C5), 3213–3220, 1982.

Weisberg, R. H., and C. Colin, Equatorial Atlantic Ocean temperature and current variations during 1983 and 1984, *Nature*, *322*(6076), 240–243, 1986.

Zimbelman, D. F., and A. J. Busalacchi, The wet tropospheric range correction: Product intercomparisons and the simulated effect for tropical Pacific altimeter retrievals, *J. Geophys. Res.*, *95*(C3), 2899–2922, 1990.

S. Arnault, J. Merle, and A. Morlière, Laboratoire d'Océanographie et de Climatologie, ORSTOM, Université Pierre et Marie Curie, Tour 14-2, 4 Place Jussieu, 75252 Paris Cedex 05, France.
Y. Ménard, Groupe de Recherche en Géodésie Spatiale, CNES, 18 avenue E. Belin, 31055 Toulouse Cedex, France.